Friedrich-Alexander-Universität
Erlangen-Nürnberg

Department für Physik
Lehrstuhl für Physik

DIPLOMARBEIT

Spatially Resolved X-Ray Spectroscopy and Modeling of the Non-Thermal Emission of the Pulsar Wind Nebula in G21.5−0.9

Philipp Willmann

23. Mai 2012

Gutachter:
1. Prof. Dr. Ch. Stegmann
2. Prof. Dr. J. Wilms

Kurzfassung

In dieser Diplomarbeit wird der Pulsarwindnebel im Supernovaüberrest G21.5−0.9 morphologisch detailliert untersucht. Daten der Satelliten *XMM-Newton* und *Chandra* wurden analysiert um eine ortsaufgelöste Röntgenanalyse durchzuführen. Dazu extrahiert man Spektren von ringförmigen Regionen, die auf den Pulsar PSR J1833−1034 zentriert sind. Mit den Ergebnissen dieser Analyse optimiert man die Parameter des in dieser Arbeit verwendeten leptonischen, radialsymmetrischen und zeitunabhängigen Modells. Dessen Ziele sind die Reproduktion der gemessenen Größen des Pulsarwindnebels im Röntgenbereich (Verlauf des Spektralindex und der Oberflächenhelligkeit) sowie eine Vorhersage für die hochenergetische γ-Strahlung, die mit dem Inversen Comptoneffekt erzeugt wurde, in der Absicht diese mit Daten vom H. E. S. S.-Experiment zu vergleichen. Die H. E. S. S.-Daten wurden analysiert und die Ergebnisse werden präsentiert. Die Berechnung der Synchrotronstrahlung mithilfe der optimierten Parameter liefert eine gute Übereinstimmung mit den Röntgendaten. Die Inverse Comptonstrahlung wird berechnet unter der Voraussetzung, dass die Leptonen, die für die Synchrotronstrahlung verantwortlich sind, auch niederenergetische Photonen mit dem Inversen Comptoneffekt zu sehr hohen Energien streuen. Der Vergleich der dadurch erhaltenen Ergebnisse mit den H. E. S. S.-Daten ergibt eine akzeptable Übereinstimmung. Eine Verbesserung des Modells ließe sich wahrscheinlich durch den Einbau einer Zeitabhängigkeit erreichen.

Abstract

In the scope of this thesis a detailed morphological study of the pulsar wind nebula in the composite supernova remnant G21.5−0.9 was carried out. In order to perform spatially resolved X-ray spectroscopy, data from the satellites *XMM-Newton* and *Chandra* were analyzed by extracting spectra from annulus-shaped regions centered on the pulsar PSR J1833−1034. The results of this analysis were used to optimize the parameters of the radially symmetric and time-independent leptonic model used in this work. Aims of the modelling are to reproduce the measured properties − the spectral index and the surface brightness − of the pulsar wind nebula in the X-ray regime and to make a prediction of the Inverse Compton radiation for the purpose of a comparison with data from a very-high-energy γ-ray experiment. An analysis of H. E. S. S. data was done and the results are presented. The calculation of the synchrotron emission with the optimized parameters yields a good agreement with the measured X-ray data. Using the assumption that the same lepton population responsible for the synchrotron radiation also scatters up low-energy photons via the Inverse Compton effect to the very high energy regime, the Inverse Compton radiation is calculated. The obtained results are compared with H. E. S. S. data and a reasonable agreement is achieved. However, including a time dependence may further improve the model.

Contents

1 Introduction

Supernova explosions belong to the most catastrophic events in the Universe. When a supernova takes place, it is in some cases possible to observe it with the naked eye for days or even weeks. The first recorded supernova, SN185, was noticed by Chinese astronomers in the year 185. After that some further “historical” supernovae were observed. According to records of many astronomers around the world, SN1006 was the brightest one while SN1054 is known for having produced the famous Crab Nebula (see Fig. 2.1). SN1987a is located in the Large Magellanic Cloud and hence represents the nearest supernova observed with modern instruments. Fig. 1.1 shows the difference between the brightness of supernova SN1987a and its progenitor star. The outcome of a core collapse supernova depends on the mass of the progenitor star and the possibilities are neutron stars or black holes.

One important discovery regarding one of the results of such an explosion was made in 1967 by Jocelyn Bell and Antony Hewish. Bell found a pulsed radio signal with constant period of 1.33 s. The first reaction was that they had discovered the signal of an extraterrestrial civilization, although Bell and Hewish did not really believe in that theory. After the discovery of more pulsed signals, the theory was discarded and in 1968 it was suggested that the pulsating star, or short pulsar, is a rotating neutron star. In the past 40 years many pulsars with different properties were discovered. In particular, young and energetic

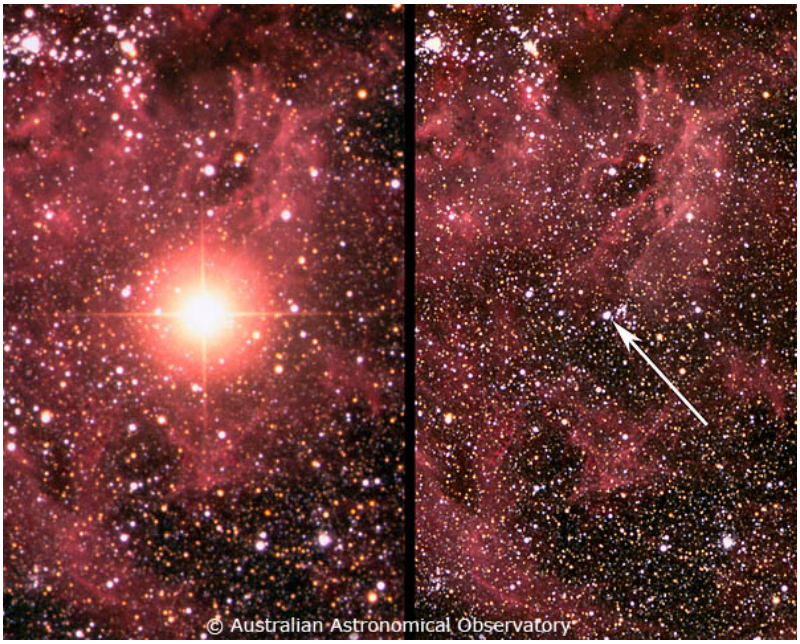

Fig. 1.1: *The supernova SN1987a is shown on the left side while the situation before the explosion can be seen on the right side. Image credit: Australian Astronomical Observatory, photograph by David Malin.*

pulsars have been found to create and power so-called pulsar wind nebulae. These objects accelerate particles over a very wide energy range which leads to radiation detectable across the whole electromagnetic spectrum and are therefore observed by astronomers to find out more about particle acceleration up to the very high energy regime.

We model pulsar wind nebulae to learn more about the properties of these objects. The leptonic model used in this thesis is radially symmetric and time-independent. This is just one possibility to model pulsar wind nebulae. Other approaches with varying degree of complexity, are models with time-dependence or semi-leptonic models. To find the values of the free parameters of the model one can apply X-ray observations of the inner part of the pulsar wind nebula and use these data to optimize the parameters by calculating the synchrotron radiation and comparing the results with the measured data. It is possible to make predictions for the γ-ray regime by calculating the radiation produced by the Inverse Compton effect using the optimized parameters. Again, one can compare the results of the modeling with data from the measurements of a γ-ray experiment, in this thesis the H. E. S. S. experiment. It is possible to constrain the magnetic field strength, an important quantity in the region around the pulsar, with the results from the modeling.
In contrast to MSH 15−5*2* and G0.9+0.1, the two pulsar wind nebulae investigated with the same model in earlier works, the pulsar wind nebula located in the supernova remnant G21.5−0.9 has an extraordinary degree of radial symmetry which justifies the application of a radially symmetric model. Pulsar wind nebulae and their radiation mechanisms in general and some properties of G21.5−0.9 are introduced in chapter 2. The observatories used to study G21.5−0.9 are described in chapter 3. The following chapter contains, as one of the main parts of this work, the detailed spatially resolved X-ray analysis mainly with the *Chandra* satellite, and the analysis of H. E. S. S. data. The second main objective of the thesis, the leptonic model applied to G21.5−0.9, is described in chapter 5. The prediction for the γ-ray regime is compared to results from the H. E. S. S. analysis. Finally a concluding summary of this work is given in chapter 6.

2 Pulsar wind nebulae

In this chapter we briefly describe Pulsar Wind Nebulae (PWNe) in general and then give some facts about G21.5−0.9, the PWN analysed and modeled in this work.

2.1 General characteristics of pulsar wind nebulae

The energy source of a PWN is the associated pulsar. Pulsars are rapidly rotating neutron stars with a strong magnetic field. Neutron stars are formed in supernova explosions where the mass of the progenitor star is above the Chandrasekhar limit of 1.4 solar masses and below a mass in the order of 25 solar masses. A pulsar loses rotational energy, which is partly used for the acceleration of electrons and positrons. These leptons move outwards as a particle wind and build a bubble-like structure around the pulsar. At the so-called termination shock the ram pressure of the wind is in balance with the internal pressure of the PWN. When the particles reach the termination shock at the radius R_ω an acceleration takes place. R_ω is defined via

$$R_\omega = \sqrt{\dot{E}/(4\pi\omega c P_{\mathrm{PWN}})}, \tag{2.1}$$

with the spin-down luminosity $\dot{E}$ (see below), the equivalent filling factor for an isotropic wind ω and the total pressure in the shocked nebular interior P_{PWN}. On the way further out the particles lose energy due to adiabatic, synchrotron and Inverse Compton processes. PWNe are visible across the whole electromagnetic spectrum. Synchrotron radiation (see section 2.2.1) is responsible for the emission from the radio to the X-ray regime. In the leptonic model applied in this thesis γ-ray emission is produced via the Inverse Compton effect (see section 2.2.2). The electromagnetic emission from the shocked particle wind is called PWN.

PWNe are commonly categorized into two types (Gaensler & Slane 2006): The prototype of a PWN surrounded by a shell-like supernova remnant (SNR), a so-called composite SNR, is G21.5−0.9 (see Fig. 2.4). The Crab Nebula (see Fig. 2.1) is an example of the other type, which does not exhibit a shell.

There are some observable properties that describe pulsars and the associated PWNe. The following account is based on the review article by Gaensler & Slane (2006).

In many cases it is possible to determine the spin period P and the period derivative $\dot{P} = \mathrm{d}P/\mathrm{d}t$ of a pulsar from observations of the pulsed signal. An important quantity is the spin-down luminosity $\dot{E} = -\mathrm{d}E_{\mathrm{rot}}/\mathrm{d}t$, which reads

$$\dot{E} = 4\pi^2 I \frac{\dot{P}}{P^3}, \tag{2.2}$$

where I is the moment of inertia of the neutron star. It is assumed that only pulsars with $\dot{P} \gtrsim 4 \times 10^{36}\,\mathrm{erg\ s^{-1}}$ can produce a PWN (Gotthelf 2004). The braking index n is defined

Fig. 2.1: *Multiwavelength picture of the Crab Nebula as an example of a PWN without a shell. Credit: X-ray: NASA/CXC/ASU/J.Hester et al.; Optical: NASA/ESA/ASU/J.Hester & A.Loll; Infrared: NASA/JPL-Caltech/Univ. Minn./R.Gehrz*

via

$$\dot{\Omega} = -k\Omega^n, \tag{2.3}$$

with $\Omega = 2\pi/P$. One can calculate the characteristic age τ_{c}, which is given by

$$\tau_{\mathrm{c}} = \frac{P}{2\dot{P}}, \tag{2.4}$$

of a pulsar when one makes the assumption that the braking index $n = 3$. τ_{c} is an estimation of the true age of a pulsar, assuming that the initial spin period P_0 is much smaller than P. However, τ_{c} overestimates the true age of a pulsar when this assumption is not valid.

The origin of the emission of non-thermal radiation from a PWN is seen in Fig. 2.2. This schematic from Aharonian & Bogovalov (2003) indicates the different regions of a PWN complex. The inner region is the magnetosphere around the pulsar where pulsed radiation from radio to γ-rays originates. Between the pulsar and the shock front is a region where γ-rays are produced via the Inverse Compton process. In the outer part, corresponding to the PWN, one detects synchrotron emission and Inverse Compton radiation from the radio to the γ-ray part of the spectrum.

2.2 Radiation mechanisms

It is possible to observe PWNe across the whole electromagnetic spectrum and thus one can perform a multiwavelength analysis. This is done to restrict models that are used to identify the accelerated particles (leptons or hadrons). The result of such an analysis can be plotted as a Spectral Energy Distribution (SED) similar to the one presented in Fig. 2.3.

In this example from Abdo et al. (2011) one can see the SED of the blazar 3C 66A with a leptonic model fit. There are two humps indicated by the data points and the model,

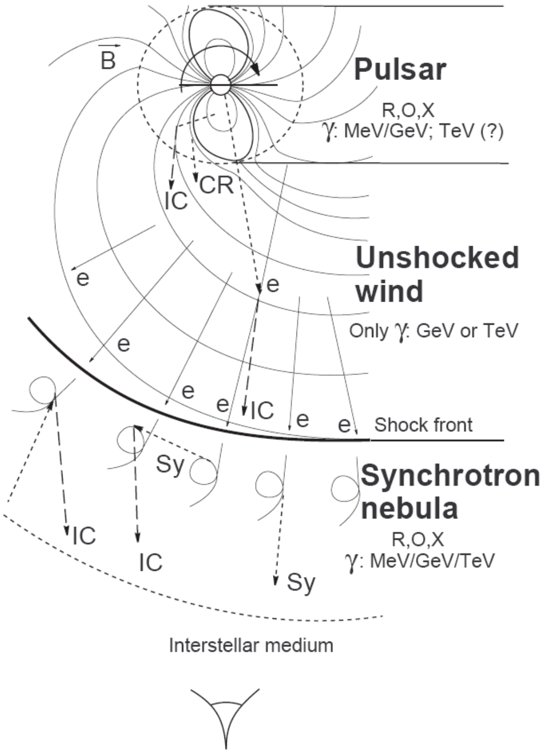

Fig. 2.2: *The origin of the radiation from a PWN complex is shown in this schematic view. The outer part, denoted as synchrotron nebula, corresponds to the region that is associated with the PWN, where synchrotron emission and Inverse Compton radiation are responsible for emission from the radio to the γ regime. The figure is taken from Aharonian & Bogovalov (2003).*

the first one reaches from the radio to the X-ray regime and the second one is in the high-energy regime. Another example for a SED is Fig. 5.3 in section 5.3 where we show a SED of G21.5−0.9. In this chapter the radiation mechanisms that produce the observed emission are described.

2.2.1 Production of X-rays

As mentioned before, the first hump in the SED in Fig. 2.3 lies in the radio to X-ray part of the spectrum. The radiation process that is responsible for this emission is synchrotron radiation. The following description is based on the review article of Blumenthal & Gould (1970).

Synchrotron radiation is produced when charged particles are deflected by a magnetic field. It can be regarded as Compton scattering off the virtual photons of the magnetic field. As a starting point we have an electron with energy $E = \gamma mc^2$ and pitch angle α (angle between velocity $\vec{v}$ and magnetic field $\vec{B}$) which spirals with an angular frequency $\Omega = eB/\gamma mc$. Deriving the energy-loss rate yields

$$-P_{\mathrm{Sy}} = \left(\frac{\mathrm{d}E_{\mathrm{e}}}{\mathrm{d}t}\right)_{\mathrm{Sy}} = -\frac{2r_0^2}{3c}\gamma^2 B^2 v^2 \sin^2\alpha, \tag{2.5}$$

with $r_0 = e^2/mc^2$ and the Lorentz factor γ. It is possible to calculate the radiation from

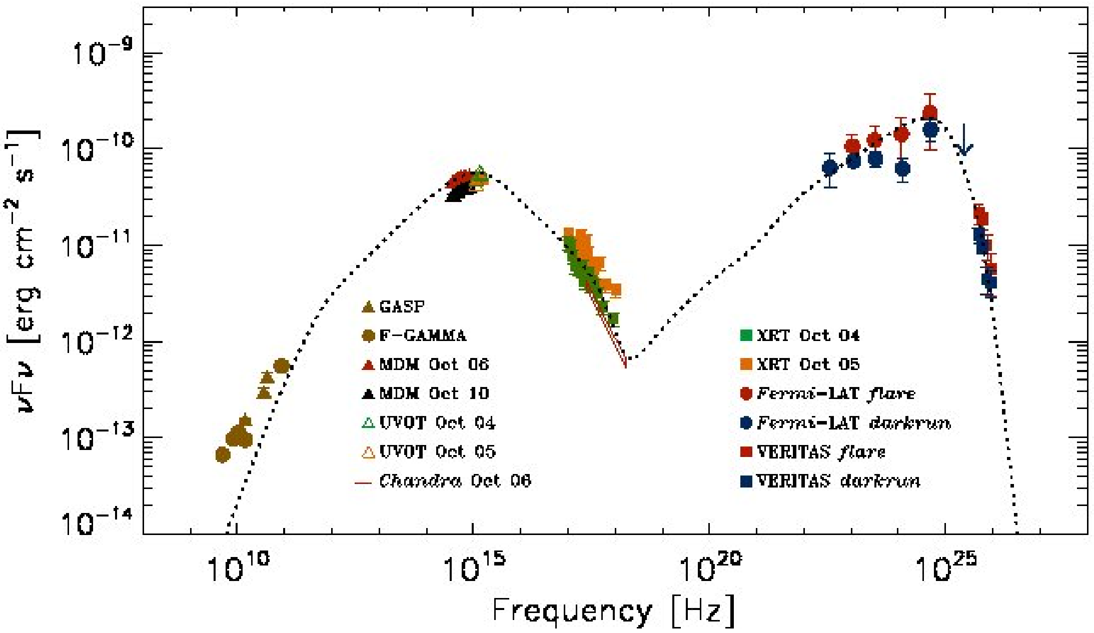

Fig. 2.3: *SED of the blazar 3C 66A as an example for a SED. The legend denotes the observations shown in the SED. The dotted line illustrates the results of a leptonic model described in the figure reference. Figure taken from Abdo et al. (2011).*

an electron for different angles. For an arbitrary pitch angle α one gets the synchrotron energy loss which is the standard formula for the synchrotron spectrum:

$$P_{\mathrm{Sy}}(\nu) = \frac{\sqrt{3}e^3 B \sin\alpha}{mc^2} \frac{\nu}{\nu_{\mathrm{c}}} \int_{\nu/\nu_{\mathrm{c}}}^{\infty} \mathrm{d}\xi \, \mathrm{K}_{5/3}(\xi). \tag{2.6}$$

ν_c is the critical frequency which is defined as

$$\nu_{\mathrm{c}} = \frac{3eB\gamma^2}{4\pi m_{\mathrm{e}} c} \sin\alpha, \tag{2.7}$$

and $\mathrm{K}_{5/3}$ is the modified Bessel function of order 5/3.

To derive the synchrotron spectrum from an electron distribution the starting points are $N_{\mathrm{obs}}(\gamma, \alpha, \vec{r}, t)\mathrm{d}\gamma\mathrm{d}\Omega_\alpha r^2\mathrm{d}r\mathrm{d}\Omega$, the total number of electrons within $r^2\mathrm{d}r\mathrm{d}\Omega$ with energy within $\mathrm{d}\gamma$ and pitch angle within $\mathrm{d}\Omega_\alpha$, and the following integration:

$$\frac{\mathrm{d}W}{\mathrm{d}\nu\mathrm{d}t} = \int\int \frac{P_{\mathrm{Sy}}(\nu) N_{\mathrm{obs}}(\gamma, \alpha, \vec{r}, t)}{\sin^2\alpha} \mathrm{d}\gamma\mathrm{d}\Omega_\alpha. \tag{2.8}$$

After relating N_{obs} with $N(\gamma, \alpha, \vec{r}, t)\mathrm{d}\gamma\mathrm{d}\Omega_\alpha$, the density of electrons at position $\vec{r}$ at time t with pitch angle within $\mathrm{d}\Omega_\alpha$ and energy within $\mathrm{d}\gamma$, one can calculate the synchrotron emission spectrum from an electron energy distribution. With the assumptions that this distribution is a power law, that there is no pitch angle dependency and that the norm k of the power-law is not time-dependent, one obtains the distribution

$$N(\gamma) = k\gamma^{-p}. \tag{2.9}$$

With some simplifications (e.g. local isotropy) one gets this final result for the synchrotron emission of a power-law electron distribution:

$$\left(\frac{\mathrm{d}W}{\mathrm{d}\nu\mathrm{d}t}\right)_{\mathrm{Sy}} = \frac{4\pi k e^3 B^{(p+1)/2}}{m_\mathrm{e} c^2} \left(\frac{3e}{4\pi m_\mathrm{e} c}\right)^{(p-1)/2} a(p)\,\nu^{-(p-1)/2}, \tag{2.10}$$

with

$$a(p) = \frac{2^{(p-1)/2}\sqrt{3}\,\Gamma[(3p-1)/12]\,\Gamma[(3p+19)/12]\,\Gamma[(p+5)/4]}{8\pi^{1/2}(p+1)\Gamma[(p+7)/4]}. \tag{2.11}$$

In equation 2.10 one sees that $\left(\frac{\mathrm{d}W}{\mathrm{d}\nu\mathrm{d}t}\right)_{\mathrm{Sy}}$ depends on ν as

$$\left(\frac{\mathrm{d}W}{\mathrm{d}\nu\mathrm{d}t}\right)_{\mathrm{Sy}} \propto \nu^{-(p-1)/2}. \tag{2.12}$$

Using $E = h\nu$ this can also be written as

$$\left(\frac{\mathrm{d}W}{\mathrm{d}E\mathrm{d}t}\right)_{\mathrm{Sy}} \propto E^{-(p-1)/2}. \tag{2.13}$$

It is possible to derive a power-law synchrotron photon spectrum ($\propto E^{-\Gamma}$) out of a power-law electron spectrum (see equation 2.9). They are related via $\mathrm{d}W = E\mathrm{d}N$, which yields

$$\left(\frac{\mathrm{d}N}{\mathrm{d}E\mathrm{d}t}\right)_{\mathrm{Sy}} \propto E^{-(p+1)/2}. \tag{2.14}$$

One can now relate the spectral index Γ of the the emitted photon spectrum to that of the electron spectrum by using the formula

$$\Gamma = \frac{p+1}{2}. \tag{2.15}$$

Because of the synchrotron radiation electrons lose energy which means that in later times there are more and more electrons with low energies and less electrons with high energies because the number of injected highly energetic electrons is not increasing over time. This phenomenon is known as synchrotron cooling.

2.2.2 Production of γ-rays

The second hump of the SED (see Fig. 2.3) is located in the high-energy part of the spectrum. The process generally considered to be responsible for this emission is Inverse Compton scattering (IC). In comparison to the Compton scattering where a photon loses energy while undergoing scattering with an electron, in the IC process an electron transfers energy to a low-energy photon. This photon can then have energies up to the γ-ray regime. Compton and Inverse Compton scattering are related by a Lorentz transformation. In the astrophysical case the photon that is up-scattered can come from various photon fields. Possible seed photon fields are the photons from the cosmic microwave background (CMB), infrared (IR) photons from local dust and photons from starlight.

The remainder of this subsection is based on the review article by Blumenthal & Gould (1970). When considering Compton scattering or Inverse Compton scattering, there are two limiting cases with an approximate expression for the cross section, the Thomson limit and the Klein-Nishina limit. In the case of the Thomson limit for Compton scattering, where the photon energy is much smaller than the electron rest mass, the Thomson cross section $\sigma_\mathrm{T} = \frac{8\pi}{3} r_0^2$ is used and one derives the following equation for the total electron energy loss rate

$$-\left(\frac{\mathrm{d}E_\mathrm{e}}{\mathrm{d}t}\right)_\mathrm{IC} = \frac{4}{3}\sigma_\mathrm{T} c \gamma^2 \epsilon_\mathrm{B}, \tag{2.16}$$

with the mean magnetic field energy density $\epsilon_\mathrm{B} = \frac{\langle B^2 \rangle}{8\pi}$.

In the case of the Klein-Nishina limit one has a total electron energy loss rate that is proportional to the logarithm of the relativistic Lorentz factor γ in contrast to the proportionality to γ^2 in the Thomson limit.

In the general case one expresses the scattered photon energy ϵ_1 in terms of the initial electron energy,

$$\epsilon_1 = \gamma m c^2 E_1. \tag{2.17}$$

Note that in this equation E_1 denotes a ratio factor and not an energy.

The general result for the scattered photon spectrum per electron is

$$\left(\frac{\mathrm{d}N_{\gamma,\epsilon}}{\mathrm{d}t\mathrm{d}E_1}\right)_\mathrm{IC} = \frac{2\pi r_\mathrm{e}^2 m_\mathrm{e} c^3}{\gamma} \frac{n(\epsilon)\mathrm{d}\epsilon}{\epsilon} \left[2q\ln q + (1+2q)(1-q) + \frac{1}{2}\frac{(\Gamma_\mathrm{e} q)^2}{1+\Gamma_\mathrm{e} q}(1-q)\right], \tag{2.18}$$

with $\Gamma_\mathrm{e} = 4\epsilon\gamma/mc^2$ and $q = E_1/\Gamma_\mathrm{e}(1-E_1)$.

The goal now is to calculate the total Compton spectrum. With a differential number of electrons $\mathrm{d}N_\mathrm{e} = N_\mathrm{e}(\gamma)\mathrm{d}\gamma$ we can calculate it by integrating equation 2.18 over ϵ and γ.

With a power-law electron energy distribution ($N_\mathrm{e}(\gamma) = K_\mathrm{e}\gamma^{-p}$) and a blackbody distribution for $n(\epsilon)$ we obtain for the total spectrum

$$\left(\frac{\mathrm{d}N_\mathrm{tot}}{\mathrm{d}t\mathrm{d}\varepsilon_1}\right)_\mathrm{IC} = \frac{r_\mathrm{e}^2}{\pi\hbar^3 c^2} K_\mathrm{e} (kT)^{(p+5)/2} F(p) \varepsilon_1^{-(p+1)/2}, \tag{2.19}$$

with

$$F(p) = 2^{p+3}\left[(p^2+4p+11)/(p+3)^2(p+1)(p+5)\right]\Gamma[1/2(p+5)]\,\zeta[1/2(p+5)], \tag{2.20}$$

and the Riemann function ζ.

From equation 2.19 it can be seen that with a power-law electron distribution one gets a power-law photon spectrum with the same index as the synchrotron spectrum.

2.3 The pulsar wind nebula G21.5−0.9

G21.5−0.9 was observed extensively across the whole electromagnetic spectrum. It was first found in radio observations and considered to be a supernova remnant (SNR) (see e.g. Becker & Kundu (1976)). Later Furst et al. (1988) suggested that there is a central pulsar after finding a centrally peaked diffuse emission in 22.3 GHz observations. G21.5−0.9 was also observed with the X-ray satellites *XMM-Newton* and *Chandra* and it was the first PWN with a detected X-ray halo (Slane et al. 2000; Warwick et al. 2001; Safi-Harb et al. 2001). In following observations a candidate for the supernova shell was revealed in the form of limb brightening of the halo (Matheson & Safi-Harb 2005; Bocchino et al. 2005).

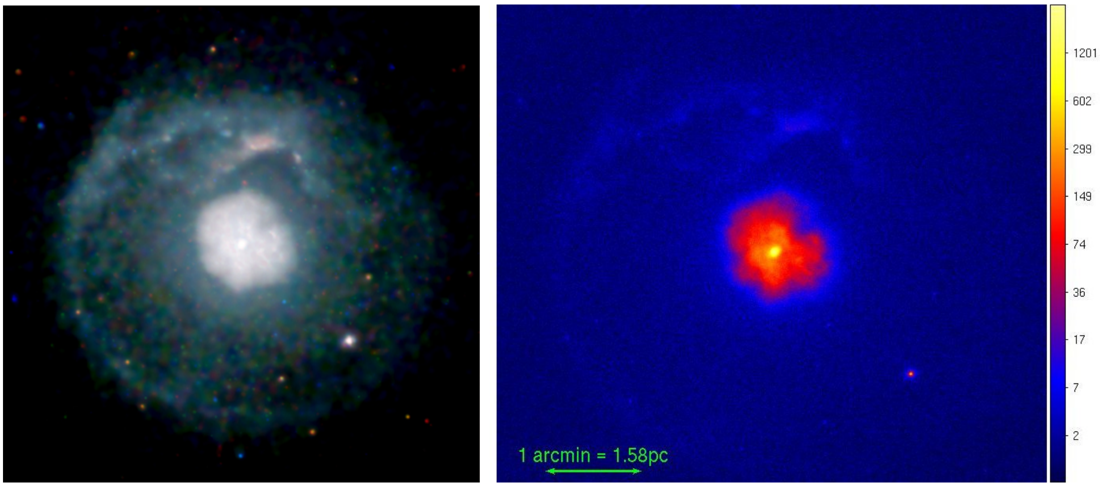

(a) *Chandra* image taken from NASA/CXC/U.Manitoba/H.Matheson & S.Safi-Harb

(b) *Chandra* image (own analysis)

Fig. 2.4: *Chandra images of G21.5−0.9. The pulsar is visible as the bright central point source with the PWN around it as well as the X-ray halo. The bright point source on the bottom right side is a foreground star and not associated with the PWN. Image (a) is an Astronomy Picture of the Day[1] from 2005. An image of our own analysis with more exposure time than in (a) is shown in (b) where the PWN is seen in red and the pulsar in yellow.*

The associated pulsar, PSR J1833−1034 ($R.A. = 18^{\mathrm{h}}33^{\mathrm{m}}33^{\mathrm{s}}.8$, $Dec. = -10°34'10''$ (J2000.0)), was discovered independently by Gupta et al. (2005) and Camilo et al. (2006) in the radio band. The properties of the pulsar that will be described next are from these two references. The pulsar has a spin period of $P = 61.86\,\mathrm{ms}$ and a period derivative of $\dot{P} = 2.0 \times 10^{-13}\,\mathrm{s\,s^{-1}}$, which implies a characteristic age of $\tau_{\mathrm{c}} = 4.8\,\mathrm{kyr}$. With a spin-down luminosity of $\dot{E} = 3.3 \times 10^{37}\,\mathrm{erg\,s^{-1}}$ PSR J1833-1034 is a highly energetic pulsar. The true age of the pulsar and hence of G21.5−0.9 is assumed to be much smaller than the characteristic age.

The distance was estimated to be $(4.7 \pm 0.4)\,\mathrm{kpc}$ by Camilo et al. (2006) and Tian & Leahy (2008) confirm this result ($d \approx 4.8\,\mathrm{kpc}$) by comparing HI spectra with ^{13}CO spectra. Bietenholz & Bartel (2008) used observations of the Very Large Array to estimate the true age and derived an age of 870^{+200}_{-150} yr so that G21.5−0.9 is one of the youngest PWNe known.

In Fig. 2.4(a) one can see a *Chandra* image of G21.5−0.9 produced by Matheson & Safi-Harb (2005). In the middle is the pulsar surrounded by the PWN. On the bottom right side there is a bright point source which is a foreground star that is not associated with the pulsar or the supernova remnant. Around the PWN one sees a halo which could be the SNR shell. The bright feature north of the PWN is known in the literature as “North Spur” (Bocchino et al. 2005) or “Northern Knot” (Matheson & Safi-Harb 2005). A picture from our own analysis is shown in Fig. 2.4(b) where you can see the PWN in red.

The latest publication on G21.5−0.9 in the X-ray regime is from Matheson & Safi-Harb (2010) who used *Chandra* data for a detailed analysis of the halo with the northern knot

---

[1] `http://apod.nasa.gov/apod/astropix.html`

and the PWN. The search for a radio counterpart for the shell-like structure seen in X-rays put forward by Bietenholz et al. (2011) remained without a positive result. G21.5−0.9 was also observed in the infrared and Zajczyk et al. (2011) conclude that infrared observations are an effective tool to study the inner structure of PWNe. They deduced a toroidal magnetic field from polarimetric observations and confirmed that synchrotron emission comes from particles which radiate in the downstream flow after acceleration at the termination shock.

3 Observatories

3.1 X-rays

In contrast to the optical or the radio part of the electromagnetic spectrum, it is not possible to observe X-rays with ground-based telescopes because the photons cannot pass the atmosphere due to photoelectric absorption. Therefore it is necessary to go above the atmosphere in order to detect X-ray emission. This is done by experiments onboard ballons or rockets and by satellites that are brought into space with rockets like the Ariane or formerly with the Space Shuttle. We concentrate on satellite experiments with imaging reflecting telescopes because of their unmatched resolution. There are other possible techniques for satellites, e.g. the position sensitive proportional counter used for the *ROSAT* mission, but the reflecting telescope technique is best suited for the type of analysis carried out in this thesis and hence will be described in the following.

The mechanism of focusing X-rays onto a detector differs from the one used in optical and infrared astronomy. Only X-ray photons that hit a mirror at small angles ($\lesssim 2^\circ$) are reflected. Otherwise the photon is absorbed or transmitted. The technique used to detect X-rays with a reflecting telescope on board of a satellite was introduced by Wolter (1952). Although there are two types of Wolter telescopes, only one type, the Wolter-I telescope, is used in currently operating X-ray satellites. In such a telescope the X-ray photons are reflected at grazing incidence angles first at a paraboloid surface and then at a hyperboloid surface. This can be seen in the schematic Fig. 3.1. Since the incidence angle is very small the effective area is also small. In order to increase the effective area, the current Wolter telescopes are not only equipped with one mirror but many nested mirror shells with the same focal length but different radii, as indicated in Fig. 3.1. This technique only works up to photon energies of some keV and the number of mirrors depends on the goal and collection area requirements of the mission. One disadvantage of such a telescope type is the so called vignetting which means that the sensitivity in the outer regions of the field of view is not as good as in the center. All modern X-ray satellites working in the low keV regime, *XMM-Newton* and *Chandra* included, employ this technique. Data from both observatories were used in this work and therefore the next sections contain a brief overview about each of them.

3.1.1 XMM-Newton

XMM-Newton (X-ray Multi-Mirror Mission) was launched on December 10th 1999 onboard an Ariane 504 rocket. It is the largest satellite ever built and brought to space by the European Space Agency (ESA). It has a length of about 10 m and a mass of 3.8 tonnes, while the solar panels give the satellite a span of 16 m. *XMM-Newton* has a 48-hour elliptical orbit with an initial apogee of 114000 km and an initial perigee of 7000 km. *XMM-Newton* consists of three x-ray telescopes and three main scientific instruments which are described later. Fig. 3.2 shows an artistic view of the satellite.

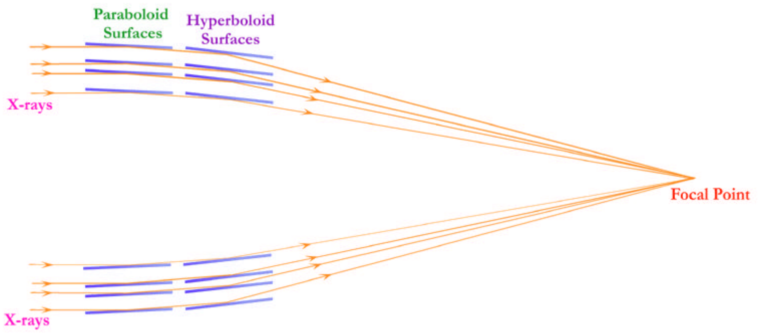

Fig. 3.1: *Schematic view of the photon path in a Wolter telescope. Image credit: NASA/CXC/S. Lee*

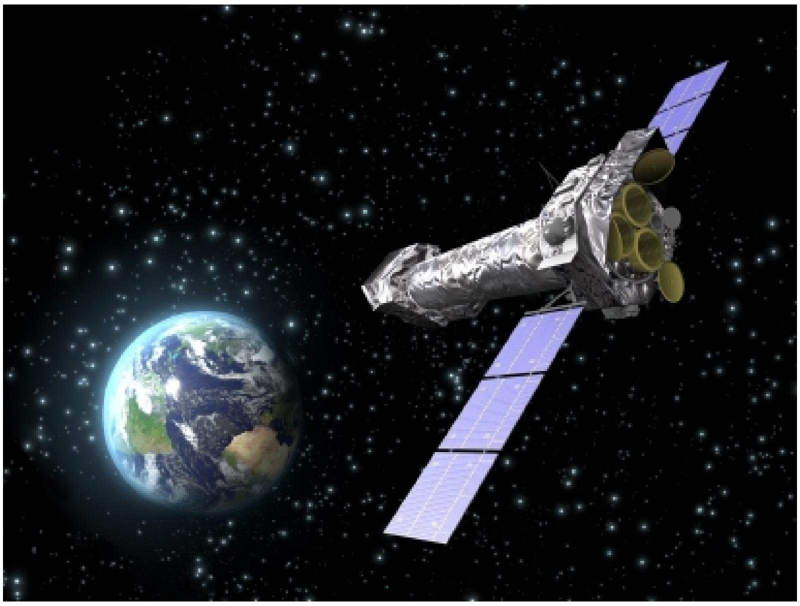

Fig. 3.2: *Artistic view of the XMM-Newton satellite. Image credit: ESA/XMM-Newton.*

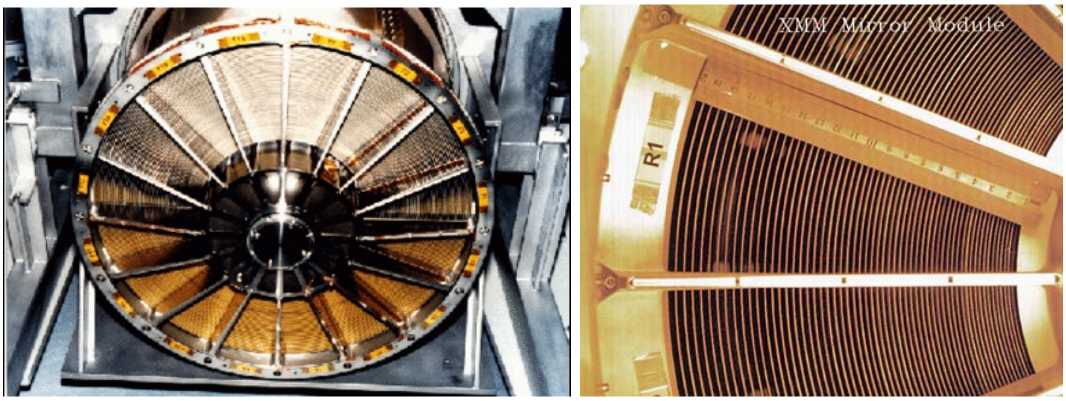

(a) *XMM-Newton* mirror module from the back, image credit: ESA

(b) Close look at the 58 nested *XMM-Newton* mirrors. Image credit: Max Planck Institute for Extraterrestrial Physics, 1998 calendar picture

Fig. 3.3: *The two photographs show XMM-Newton mirrors. (a) is a view from the back of an XMM-Newton mirror module and (b) a close-up on the* 58 *nested mirrors.*

The three telescopes each consist of 58 grazing-incidence Wolter mirrors nested in a coaxial and cofocal configuration. Photographs of an *XMM-Newton* are shown in Fig. 3.3. In these pictures the nested mirrors characteristic for a Wolter telescope can be seen. Each segment in Fig. 3.3(b) is about 1 mm thick and the narrow gap between the segments indicate the small incident angle necessary for the X-ray photons.

The three scientific instruments are the Optical Monitor (OM), the Reflection Grating Spectrometer (RGS) and the European Photon Imaging Camera (EPIC). The OM is a 2 m long conventional telescope sensitive in the optical and UV regime to provide complementary data of the source[1]. Two of the three Wolter telescopes have a grating structure on their mirror modules which deflects about 40 % of the incoming photons before they reach the EPIC-MOS cameras (see below) to a secondary CCD, the RGS[2]. This instrument provides information about the K-shell transition of elements like oxygen and iron and allows high-resolution energy measurements.

In this thesis only data from the EPIC instrument were used. As was already mentioned two of the three telescopes are equipped with MOS (Metal Oxide Semi-conductor) CCD arrays and the third is equipped with a pn CCD array. Each of the MOS cameras (see Turner et al. 2001) consists of seven front-illuminated CCDs with the central CCD located at the focal point on the optical axis of the telescope while the others are stepped towards the mirror by 4.5 mm. The pn camera (see Strüder et al. 2001) was specifically developed for *XMM-Newton* and is composed of twelve back-illuminated pn CCDs which are hosted on a single wafer. The photons hit the CCD from the rear side and produce electron-hole pairs. Before recombination the pairs are separated by strong electric fields. Due to this design the pn camera has a higher sensitivity than the MOS cameras.

---

[1] for more information see Mason et al. (2001)

[2] for more information see den Herder et al. (2001)

Fig. 3.4: *Artistic view of the Chandra satellite. Image taken from NASA/CXC/NGST.*

3.1.2 Chandra

The NASA launched *Chandra* (Weisskopf et al. 2002) on July 23rd 1999. With a length of 13.8 m and a weight of 4.8 tonnes, it is the largest satellite ever transported by a Space Shuttle. The satellite has a highly elliptical 63.5 hours orbit to achieve a high observing efficiency with an apogee of 140000 km and a perigee of 10000 km. In contrast to *XMM-Newton* with its three telescopes *Chandra* works with only one telescope. The *Chandra* telescope consists of four pairs of nested mirrors which are shown in Fig. 3.1. One can see an artistic view of the satellite in Fig. 3.4.

The instruments of *Chandra* are described in the following. *Chandra* has two transmission gratings, the High Energy Transmission Grating (HETG) and the Low Energy Transmission Grating (LETG), and two focal plane instruments, the High-Resolution Camera (HRC) and the Advanced CCD Imaging Spectrometer (ACIS). The gratings can be moved into the light path and enable high-resolution spectroscopy. The HRC is composed of two Micro-Channel Plates which consist of millions of glass tubes each. The camera is well suited for imaging hot matter in supernova remnants and galaxies and for the detection of very faint sources.
We used only data from the ACIS instrument (Garmire et al. 2003) which is comprised of ten CCDs which are especially designed for X-ray detection. They are arranged in a square array of four front-illuminated CCDs and a linear array of the remaining six CCDs (two back-illuminated and four front-illuminated CCDs). The instrument with the mounting structure is seen in Fig. 3.5. The square array is called ACIS-I, for imaging, and the linear array ACIS-S, for spectroscopy. It is only possible to use up to six CCDs at the same time because of the used electronics. The nominal focal plane temperature is -120°C but observations also take place at higher temperatures, which has to be accounted for in the analysis.

3.2 γ-ray observations with the H. E. S. S. experiment

In the γ-ray regime the situation is similar to the one in the X-ray part. One cannot observe γ-rays with telescopes on the ground directly because the photons are absorbed

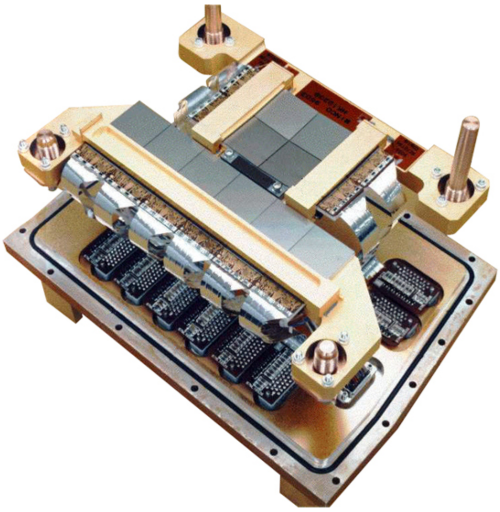

Fig. 3.5: *The Advanced CCD Imaging Spectrometer (ACIS) shown with the mounting structure. The square array and the linear array can be clearly identified. Image taken from CfA/SAO/NASA.*

on their way through the atmosphere. On the one hand this is very helpful for life on Earth because γ-rays are so energetic that they can harm life on Earth. On the other hand it makes it more difficult to detect them. One solution is again to go above the atmosphere and make use of satellites, which is done with the *Fermi Gamma-ray Space Telescope*. Another possibility is to exploit the Cherenkov effect and build ground-based telescopes which observe the light emitted by the secondary particles in extensive air-showers that are produced when γ-rays strike the atmosphere. This technique is used in the very-high-energy regime where the effective area of satellite experiments is too low in comparison to the photon flux. Currently there are three large experiments which work with the so-called “Imaging Atmospheric Cherenkov technique” (IACT): H. E. S. S., MAGIC and VERITAS. Modern IACT experiments consist of more than just one telescope to exploit the advantages of stereoscopic observations, such as the improvement of the reconstructed direction of the primary photon. We used data from the H. E. S. S. experiment and describe the experiment after a short general introduction to the IACT.

IACT is the method used in modern γ-ray astronomy to study photons with the highest energies. The basis of this technique is the Cherenkov effect. A charged particle moving with a velocity greater than the speed of light in the traversed medium causes the emission of electromagnetic radiation, the Cherenkov radiation. This light is emitted in a cone with an opening angle depending on the altitude.
When γ-rays strike the atmosphere, they produce secondary particles and the charged leptons created this way can produce Cherenkov light. Assuming the first interaction took place at an altitude of 10 km the light on the ground illuminates an area with a radius of about 120 m. This can be seen in the schematic Fig. 3.6 where an air-shower produced by a 300 GeV photon and for comparison a proton-induced air-shower of somewhat higher energy are shown. In the inset on the left side of the sketch the stereoscopic reconstruction of the direction of the initial particle is indicated for the case of two telescopes.

In this thesis data from the H. E. S. S. (High Energy Stereoscopic System) experiment are used. The experiment is located in the Khomas Highland in Namibia on the southern hemisphere at an altitude of about 1800 m a.s.l.. The site was chosen since it suffers

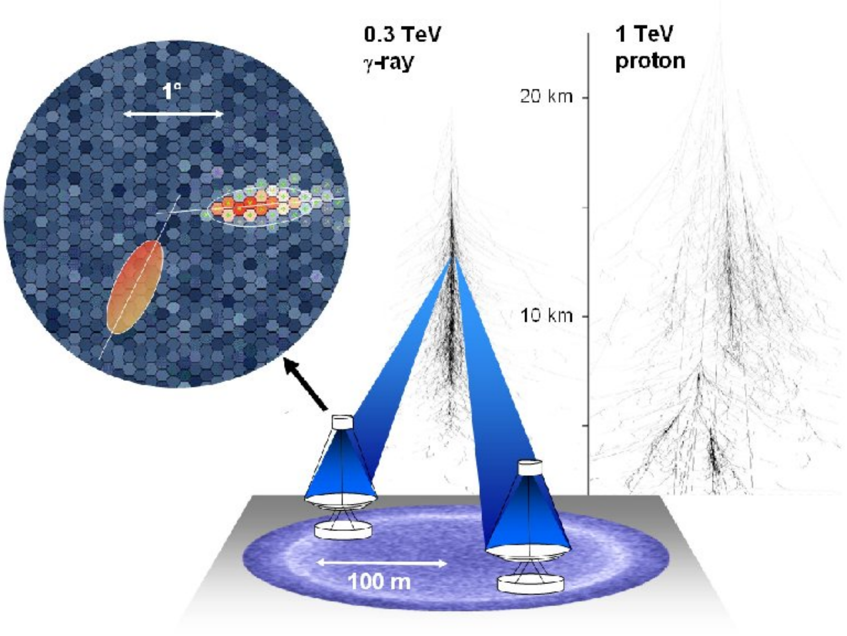

Fig. 3.6: *Schematic view of a Cherenkov cone produced by a photon-induced air shower induced by a photon. For comparison a proton-induced air shower is shown on the right side. In the circle on the left side the reconstruction of the direction of the particle can be seen. Image taken from Hinton & Hofmann (2009).*

only very little background light contamination. The experiment consists of four “phase I” telescopes with a diameter of 13 m and a fifth telescope under construction with a diameter of 28 m. The four telescopes are arranged in a square of 120 m and take data since 2003. The whole array can be seen in Fig. 3.7. Each telescope can point to any position in the sky. This is achieved by an azimuthal mounting structure that can be moved on a circular base and carries the dish which can be elevated up to 90°. Each of the telescopes consists of 382 mirror segments with a total mirror area of 107 m^2. With the above-mentioned stereoscopic technique it is possible to reconstruct particles with energies between about 100 GeV and 100 TeV.

Fig. 3.7: *The H. E. S. S. array in Namibia with the four* 13 m *telescopes and the new central* 28 m *telescope. The four smaller telescopes are arranged in a square of* 120 m *length.*

4 Data analysis

This chapter describes the analyses of data sets from the two X-ray satellites and the H. E. S. S. experiment introduced in the previous chapter. The first section deals with the analysis of *XMM-Newton* data and the second section with the analysis of the *Chandra* data. The analysis of the H. E. S. S. data and the results obtained in the analysis are shown in the last section.

4.1 *XMM-Newton*

In the following, the analysis of the *XMM-Newton* data set is described.

4.1.1 Observations

Seven observations of G21.5−0.9 dating from the years 2000 and 2001 are available from the *XMM-Newton* observation log browser[1](Observation IDs: 0122700101, 0122700201, 0122700301, 0122700401, 0122700501, 0122700801, 0122701001). However, because six of these observations were taken with a large offset with respect to the source, we selected only one, namely 0122700101, with 30 ks observation time. During this observation the medium filter[2] was used for all instruments. The two MOS cameras were operating in the full frame mode while the pn camera was in extended full frame mode.

4.1.2 Analysis

The *XMM-Newton* data were analyzed using the Science Analysis System (SAS), version 9.0.0[3], as well as tools from the FTOOLS package (Blackburn 1995) and ISIS, the Interactive Spectral Interpretation System, version 1.6.1-43. The analysis follows the steps outlined in the diploma thesis of M. Holler (2010) and in Holler et al. (2012).

At first, the event list was filtered for high background flaring activity by selecting good time intervals (GTI). This was done by applying a maximum count threshold to the high energy lightcurve ($7 - 15\,\mathrm{keV}$) of the complete field of view because the mirror reflectivity is quite low in this energy range and therefore one sees mainly background events. The values of 6 background counts per second for the pn camera and 2 for the MOS cameras were chosen. To make sure that only good single and multiple events are selected we used the options FLAG=0 (single) and PATTERN ≤ 4 for pn and ≤ 12 for MOS (multiple).

---

[1] `http://xmm2.esac.esa.int/external/xmm_obs_info/obs_view_frame.shtml`

[2] There are three different filters available: thin, medium or thick. They are necessary to prevent optical and UV photons from reaching the CCD chip. This information comes from Lumb et al. (2012) and for more information the reader is referred to this reference.

[3] provided by the *XMM-Newton* Science Operations Centre

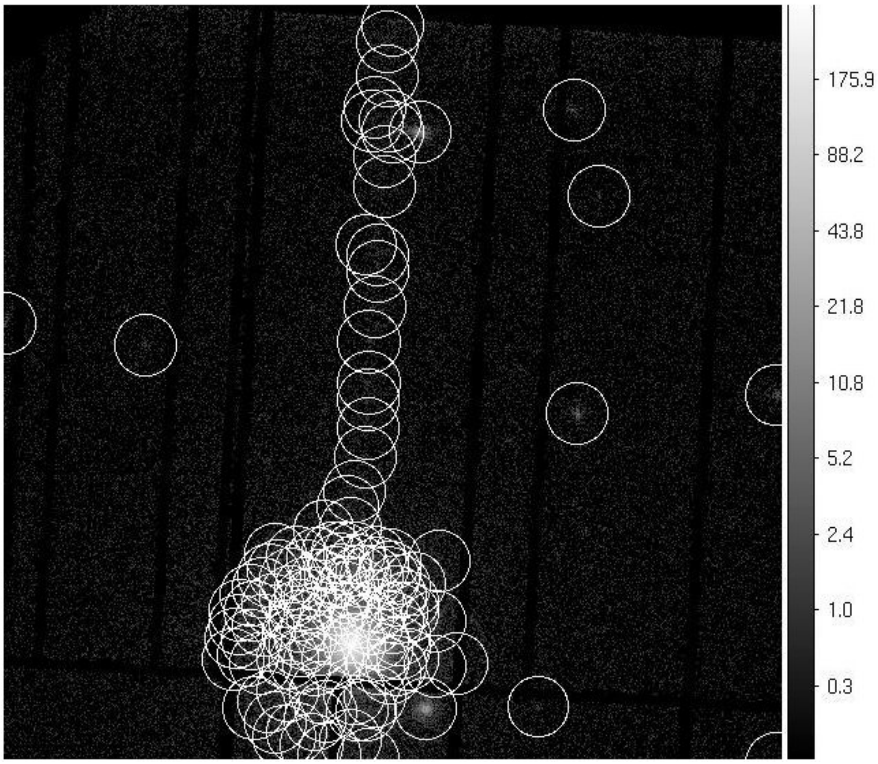

Fig. 4.1: *Results obtained from the source detection algorithm for the pn observation. The white circles are detected sources and the jet-like feature is due to OoT events. The PWN can be seen at the bottom of the image.*

There was no need for a pile-up correction[4] because of the extent of the source and its moderate brightness.

Before defining a background region the *edetect-chain* workaround (from the SAS Cookbook[5]) was used to do a source detection. The result for the pn camera is shown in Fig. 4.1. The image contains a jet-like feature comprised of the white circles which represent detected sources found by the algorithm. This is due to OoT events which are events that are registered during the readout of the CCD where the charge is shifted to the readout node. The effect is a broadening of spectral features and a band of events with wrongly reconstructed position. To correct for these effects and to get a clean spectrum the steps described in the "Users Guide to the XMM-Newton Science Analysis System", Issue 8.0, 2011 (ESA: XMM- Newton SOC) and the *XMM-Newton* SAS homepage[6] were followed. The first step is to generate an OoT events list. Then one applies all the steps of the analysis of the observation which will be described below to this event list and in the end one subtracts the OoT event spectrum from the observation spectrum in order to get a clean spectrum. The background region was defined outside of these circles as can be seen in Fig. 4.2 in a way which ensures that the on and off regions are located on the same CCD chip.

Instead of the standard analysis for *XMM-Newton* data we used the weighting method of Arnaud et al. (2001) to properly correct for the vignetting of the telescope and the

---

[4] Pile-up means the counting of more than one photon as one. This can happen if some photons hit the CCD at the same place between two read-outs

[5] `http://heasarc.gsfc.nasa.gov/docs/xmm/abc/`

[6] `http://xmm.esa.int/sas/current/documentation/threads/EPIC_OoT.shtml`

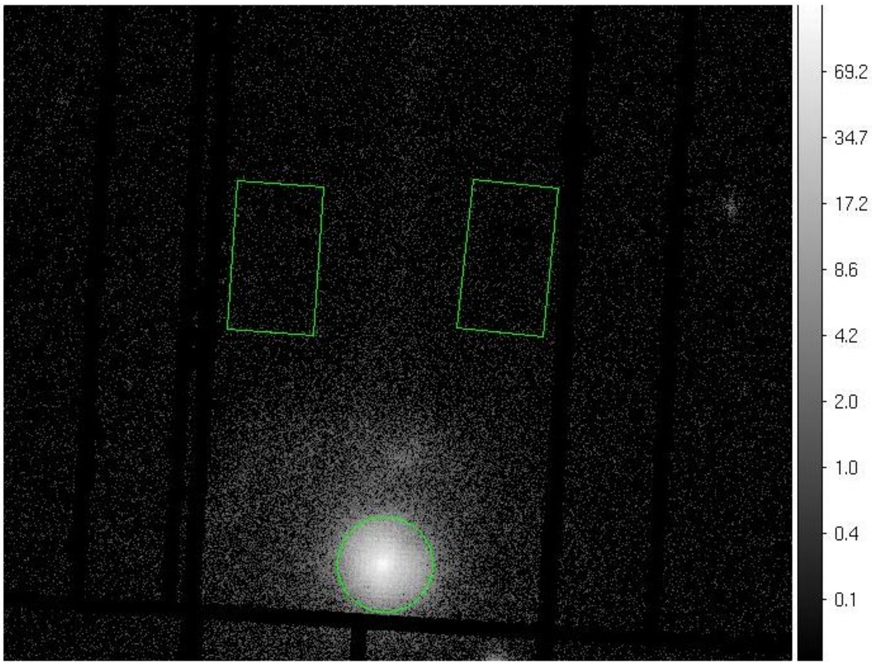

Fig. 4.2: *Count map for the pn observation. The two background regions are encompassed by green rectangles and the PWN is marked by the green circle. The same regions were used for the MOS observations.*

particle background subtraction method of Majerowicz et al. (2002). As the last step of the analysis a significance binning was done, grouping channels to achieve a minimum significance of 5 per bin.
The spectra obtained in this analysis are fitted simultaneously with the *Chandra* spectra, as will be described in section 4.2.2.

4.2 *Chandra*

This section explains in detail the analysis of the *Chandra* data. The first subsection, 4.2.1, specifies the used observations while in subsection 4.2.2 the results of the simultaneous fit of the *XMM-Newton* and *Chandra* data are shown which will be compared to the results of the modeling in section 5.2.

4.2.1 Observations

G21.5−0.9 is a calibration target for *Chandra*. Therefore it was regularly observed over the years with the Advanced CCD Imaging Spectrometer (ACIS) and the High Resolution Camera (HRC). Matheson & Safi-Harb (2010) made use of 65 ACIS and 15 HRC observations for their variability study and 56 ACIS observations for their spectroscopic analysis. For the spectral analysis presented in this work, 66 ACIS observations, listed in Table 4.1, with a total exposure time of about 586 ks were used. The whole data set of 76 observations comprises of observations taken at different CCD temperatures (-120°C, -110°C, -100°C) and also different offset angles. We excluded the data taken at -100°C because one cannot correct them for charge transfer inefficiency (CTI)[7] and three observations (IDs: 1432, 1842, 1843) because of the large offset.

4.2.2 Analysis

The data were analyzed using the CIAO software package version 4.3 and ISIS version 1.6.1-43. Some of the images which are shown in the following were made with the *SAOImage ds9* tool (Joye & Mandel 2003). As recommended by the Chandra X-Ray Center (CXC), we generated spectra for each observation and analyzed them simultaneously. There are two event files available, the level-1 event file which is the raw data file, and the level-2 event file which was processed with the up-to-date analysis software at the time of the observation. The CXC recommends to create a new level-2 event file from the level-1 file using the current software and calibration.

Therefore we started the analysis with the level-1 event file and used the CIAO tools *acis_process_events*, with `apply_tgain` and `apply_cti`, and *dmcopy*, with status=0 and grade=6 to have only good single and multiple events, to create a level-2 event file. Additionally we generated a new bad pixel file with the tool *acis_run_hotpix*. The next step was to use GTI to remove background flare events. This is done by first using *dmcopy* to filter for events in the energy range of $9 - 12\,\mathrm{keV}$ and then using the tool *dmextract* to create a lightcurve from background events with a bin time of 50 seconds. *dmgti* was applied with a maximum count rate threshold of 4 and with this new GTI file the level-2 event file is filtered, which is again done with *dmcopy*. The obtained filtered event file was the basis for the rest of the analysis.

In the first part of the analysis the whole PWN was analyzed while in the second part G21.5−0.9 was divided in eight annuli to do a spatially resolved analysis.

Analysis of the entire PWN

For the first part a circle including the whole PWN centered on the position of PSR J1833-1034 ($R.A. = 18^{\mathrm{h}}33^{\mathrm{m}}33^{\mathrm{s}}.8$, $Dec. = -10^\circ34'10''$ (J2000.0)) was cut out (*dmcopy*) which can be seen in Fig. 4.3. The radius of this circle is $36''$ and was chosen because of the X-ray count maps. One also needs a well-chosen background region. The region should be on the same chip as the PWN to ensure the same CCD type (front- or back-illuminated) in order to reduce the systematic error. To accomplish that for every observation, four background regions of the same size were defined, which are seen in Fig. 4.4. Those regions are located outside of the halo and have the same distance to the pulsar. To decide which of these regions is chosen it is checked for each observation which background region is on the same CCD and the first one that fulfils the requirement is selected. A source detection was done with the tool *wavdetect* where a scale parameter, determining the source size, up to 512 was used and the sources found with the algorithm were excluded from the background region.

Now it was possible to extract a spectrum. To do this one has to check whether the observation was taken at -120°C or -110°C and whether it was on a front- or back-illuminated CCD. For the case of observations taken on a back-illuminated chip or observations with

---

[7] CTI means the loss of charge during the readout. This can happen because the charge is moved pixel by pixel to the readout point and on this way there is the possibility of a transition to the conduction band in so-called traps, i.e. special states in the lattice (after `http://cxc.harvard.edu/ciao/dictionary/cti.html`).

Table 4.1: *Chandra observations used for the analysis with net exposure times.*

Detector	Time (ks)	Observation ID (Date, net exposure time in ks)
ACIS-I, -110°C	101.7	1233 (1999 Nov 5, 14.18), 1441 (1999 Nov 15, 9.17), 1442 (1999 Nov 15, 9.77), 1443 (1999 Nov 15, 9.78), 1772 (2000 Jul 5, 7.51), 1773 (2000 Jul 5, 7.32), 1774 (2000 Jul 5, 7.32), 1775 (2000 Jul 5, 7.32), 1776 (2000 Jul 6, 7.32), 1777 (2000 Jul 6, 7.32), 1778 (2000 Jul 6, 7.32), 1779 (2000 Jul 6, 7.32)
ACIS-I, -120°C	156.5	1551 (2001 Mar 8, 9.19), 1552 (2001 Jul 13, 10.44), 1719 (2000 May 23, 7.74), 1720 (2000 May 23, 7.64), 1721 (2000 May 23, 7.67), 1722 (2000 May 23, 7.67), 1723 (2000 May 23, 7.67), 1724 (2000 May 24, 7.67), 1725 (2000 May 24, 7.67), 1726 (2000 May 24, 7.66), 1841 (200 Sep 14, 8.1), 2872 (2002 Sep 13, 9.97), 3473 (2002 May 16, 9.67), 3692 (2003 May 16, 9.68), 3699 (2003 Nov 9, 9.83), 4354 (2003 May 20, 9.98), 4355 (2003 May 20, 9.56), 5158 (2005 Feb 26, 10.13), 5165 (2004 Mar 26, 9.68), 6070 (2005 Feb 26, 9.56), 6740 (2006 Feb 21, 9.96), 8371 (2007 May 28, 10.04)
ACIS-S, -110°C	69	1433 (1999 Nov 15, 15.16), 1434 (1999 Nov 16, 9.77), 1769 (2000 Jul 5, 7.52), 1770 (2000 Jul 5, 7.32), 1771 (2000 Jul 5, 7.32), 1780 (2000 Jul 5, 7.32), 1781 (2000 Jul 5, 7.32), 1782 (2000 Jul 5, 7.32)
ACIS-S, -120°C	174.8	1553 (2001 Mar 18, 10.24), 1554 (2001 Jul 21, 9.5), 1716 (2000 May 23, 7.84), 1717 (2000 May 23, 7.63), 1718 (2000 May 23, 7.67), 1727 (2000 May 24, 7.84), 1728 (2000 May 24, 7.64), 1729 (2000 May 24, 7.66), 1838 (2000 Sep 2, 7.96), 1839 (2000 Sep 2, 7.76), 1840 (2000 Sep 2, 7.76), 2873 (2002 Sep 14, 9.96), 3474 (2002 May 16, 9.63), 3693 (2003 May 16, 10.29), 3700 (2003 Nov 9, 9.66), 4353 (2003 May 15, 9.48), 5159 (2004 Oct 27, 9.96), 5166 (2004 Mar 14, 10.14), 6071 (2005 Feb 26, 9.76), 6741 (2006 Feb 22, 9.96), 8372 (2007 May 29, 10.14), 10644 (2009 Jun 1, 10.03), 10645 (2009 Jun 1, 10.13), 10646 (2009 Jun 1, 10.03)

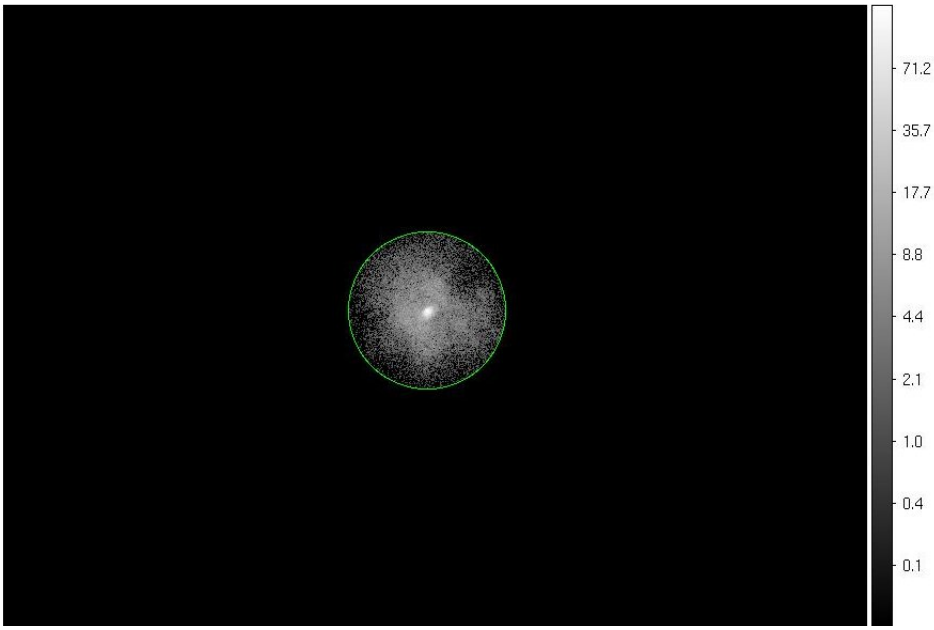

Fig. 4.3: *Chandra count map from one observation (Observation ID: 1433) showing the circular region of radius* $36''$ *that is used to analyze the PWN.*

a temperature of -120°C, one can use the tool *specextract* which combines some tools (*dmextract*, *mkwarf*, *mkacisrmf*, *dmgroup*). In the case of a front-illuminated CCD and a temperature of -110°C it is not possible to use *specextract* because one of the used tools (*mkacisrmf*) fails with an error. Therefore one checks each observation for the used temperature and CCD and in the latter case a workaround is done with the same tools as in *specextract* but *mkacisrmf* is replaced by *mkrmf*.[8]
With the spectra for each observation, ISIS was used to do a simultaneous fit of all observations with an absorbed power-law model. The analysis was done in the energy range from 1 to 10 keV. We used the abundances from Wilms et al. (2000) and the cross-sections from Verner et al. (1996). The absorption model was *tbnew* and we used the *cflux* command because we are interested in the unabsorbed energy flux and its errors. So the fit was done with $tbnew(1) * cflux(Isis\_Active\_Dataset, powerlaw(1))$ and a gainshift correction. Gainshift is an effect which occurs due to CTI. Depending on the position of the source on the CCD chip with respect to the readout, the amount of charge that is read out is smaller than the amount of charge that is deposited in the CCD. This is partially taken into account in the tool *acis_process_events*, but may lead to a distortion of the spectrum. Therefore a kernel was added to correct for the gainshift. The slope of the first loaded observation was frozen and the other slopes were fitted to take the gainshift into account. For more information about the gainshift correction the reader is referred to the dissertation of M. Hanke (2011).

For the analysis of the whole PWN we fitted all spectra obtained from *Chandra* and *XMM-Newton* data. The respective spectra together with the fit are shown in Fig. 4.5. The *Chandra*, *XMM-Newton* MOS and *XMM-Newton* pn observations are superimposed. The latter is the single line on top due to the higher sensitivity of the pn camera. Because of the loss due to the grating spectrometer the MOS observations lie on the same level

---

[8] See `http://cxc.harvard.edu/ciao/why/mkacisrmf.html`, section “Using Consistent Calibration”, −110° data.

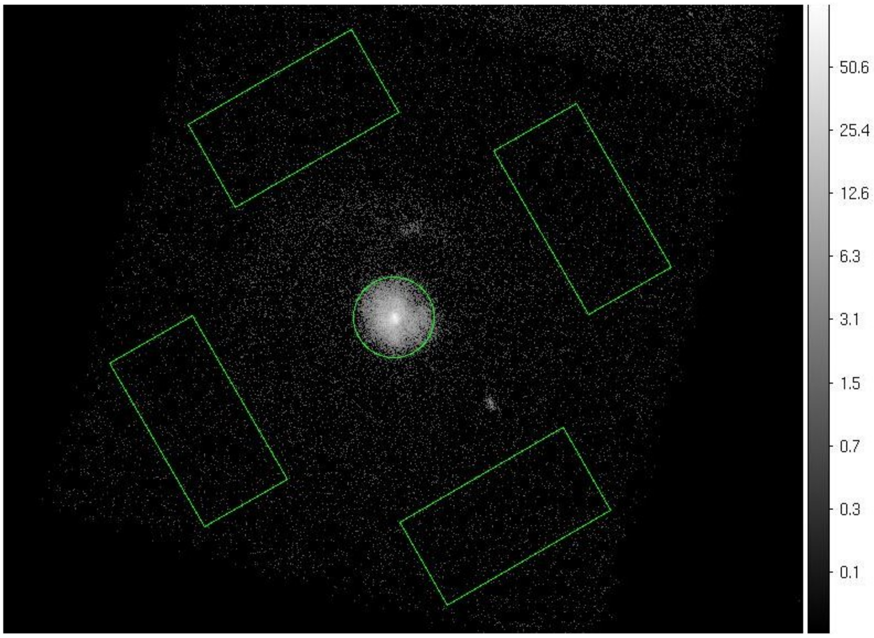

Fig. 4.4: *Chandra count map from one observation (Observation ID: 1434) showing the four background regions around the PWN.*

as the *Chandra* ACIS observations. As results of the fit, we obtained a flux of $(80.54 \pm 0.11) \times 10^{-12}\,\mathrm{erg\,cm^{-2}\,s^{-1}}$, an index of 1.772 ± 0.007, a reduced χ^2 of 1.24 and a value of $(3.24 \pm 0.01) \times 10^{22}\,\mathrm{cm^{-2}}$ for the absorption column density nH, which is related to the amount of matter in the line of sight. The value for nH was fixed for the rest of the analysis and it is higher compared to previously published analyses. This can be explained with the used abundances and cross-sections. If we use the standard abundances (Anders & Grevesse 1989) and standard cross-sections (Balucinska-Church & McCammon 1992) of ISIS we obtain a value of $2.21 \times 10^{22}\,\mathrm{cm^{-2}}$ which equals the value of nH from Matheson & Safi-Harb (2010). We took the value obtained with the abundances from Wilms et al. (2000) because they made use of the most precise measurement until now. Since Wilms et al. (2000) adopted the cross-sections of Verner et al. (1996) for their abundances we also use Verner et al. (1996).

Spatially resolved analysis

For the second part where the PWN is divided in eight annuli the procedure is the same. The differences are that the annuli instead of the whole PWN were used and due to the small size of the annuli and the angular resolution of *XMM-Newton* only data from *Chandra* were selected for this analysis. The innermost $4''$ were excluded because the pulsar itself is not interesting for the analysis and the innermost radius should be safely larger than the distance from the pulsar to the termination shock. Then we decided to use steps of $4''$ resulting in 8 annuli. This number seems appropriate considering the good statistical base and the sub-arcsecond angular resolution provided by the *Chandra* observations. Fig. 4.6 presents the geometry of the annuli and table 4.2 contains the values of the inner and outer radii of the individual annuli.

A simultaneous fit with ISIS for each annulus, in the same way as the fit for the PWN, was

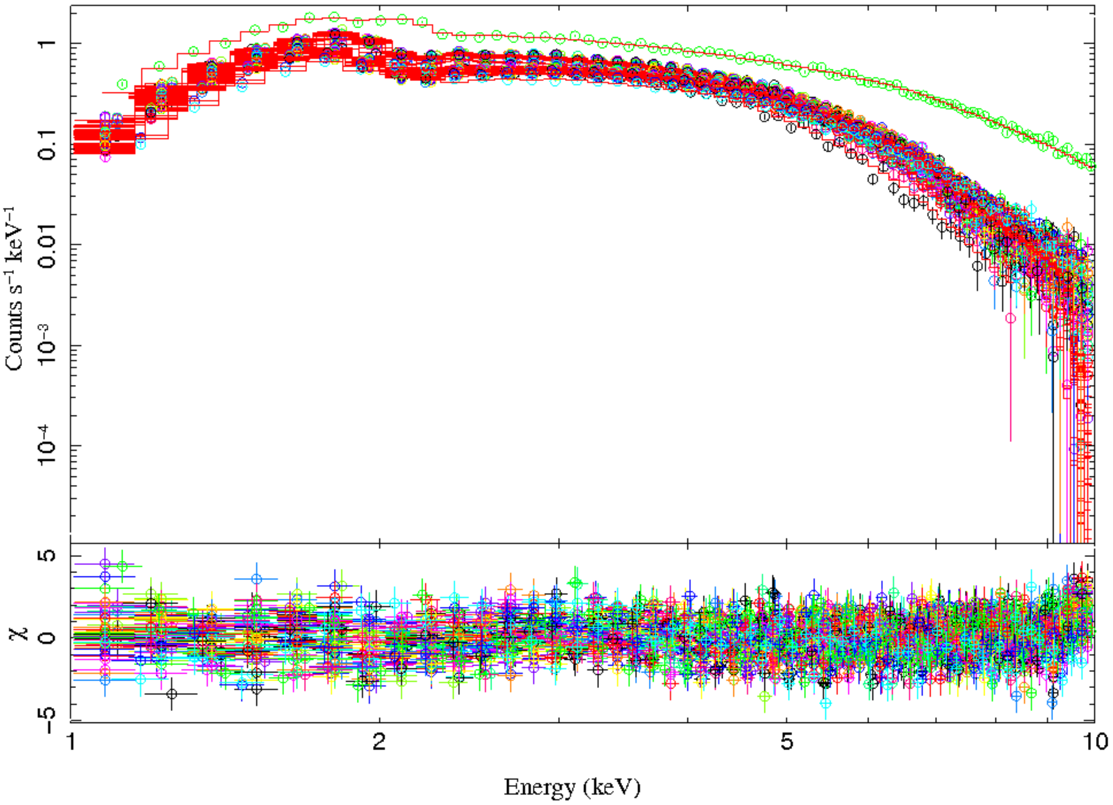

Fig. 4.5: *The spectral fit of all observations (66 ACIS Chandra and 1 XMM-Newton) of the PWN is shown. Due to its higher sensitivity, the EPIC-pn camera yields higher count rates and hence the corresponding spectrum stands out as the single line on top.*

Table 4.2: *Properties of the 8 annuli used for the analysis.*

Annulus #	1	2	3	4	5	6	7	8
Inner Radius [arcsec]	4	8	12	16	20	24	28	32
Outer Radius [arcsec]	8	12	16	20	24	28	32	36

done. The same abundances and cross-sections, as well as the same function was used. The value for nH was fixed to the one obtained in the PWN fit as mentioned before. The results of the X-ray analysis of the annuli are shown in table 4.3. The spectral index Γ and the surface brightness as the main results are also plotted in Fig. 4.7 and Fig. 4.8.

Fig. 4.7 shows the spectral index Γ as a function of angular distance to the pulsar. The index increases with the distance as expected because of loss due to adiabatic and synchrotron processes which is also known as the cooling effect (see section 2.2.1).

In Fig. 4.8 the surface brightness is plotted as a function of angular distance to the pulsar. The surface brightness decreases with increasing distance, which is already apparent from the count map in Fig. 2.4(b). (Note that due to the large exposure and the consequential good statistics the error bars are small and hence barely discernible in the surface brightness plot.)

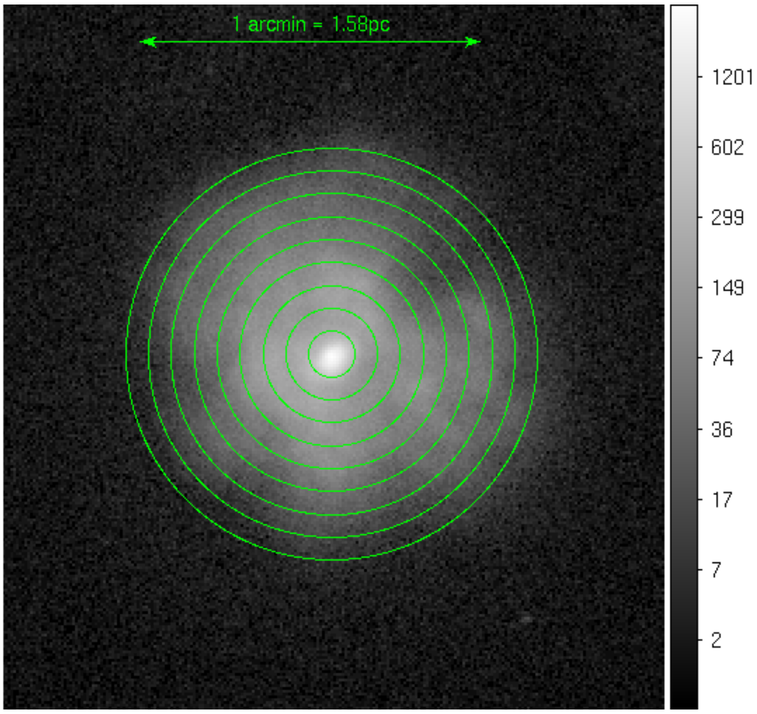

Fig. 4.6: *Chandra count map of the PWN with the eight annuli centered on the pulsar position.*

Table 4.3: *Results of the Chandra data analyses of the annuli.*

Annulus	Γ	Flux$^{(*)}$ (10^{-12} erg cm^{-2} s^{-1})	Surface Brightness (10^{-15} erg cm^{-2} s^{-1} arcsec^{-2})	red. χ^2
1	1.571 ± 0.016	9.89 ± 0.05	65.62 ± 0.34	1.19
2	1.693 ± 0.013	12.83 ± 0.05	51.05 ± 0.18	1.11
3	1.766 ± 0.013	12.80 ± 0.05	36.37 ± 0.13	1.08
4	1.858 ± 0.015	10.52 ± 0.04	23.26 ± 0.09	1.03
5	1.982 ± 0.016	7.93 ± 0.04	14.36 ± 0.06	1.08
6	2.044 ± 0.017	6.44 ± 0.03	9.86 ± 0.05	1.06
7	2.125 ± 0.020	4.48 ± 0.03	5.93 ± 0.04	1.04
8	2.195 ± 0.027	2.61 ± 0.03	3.05 ± 0.03	1.11

$^{(*)}$ Energy range $1-10$ keV

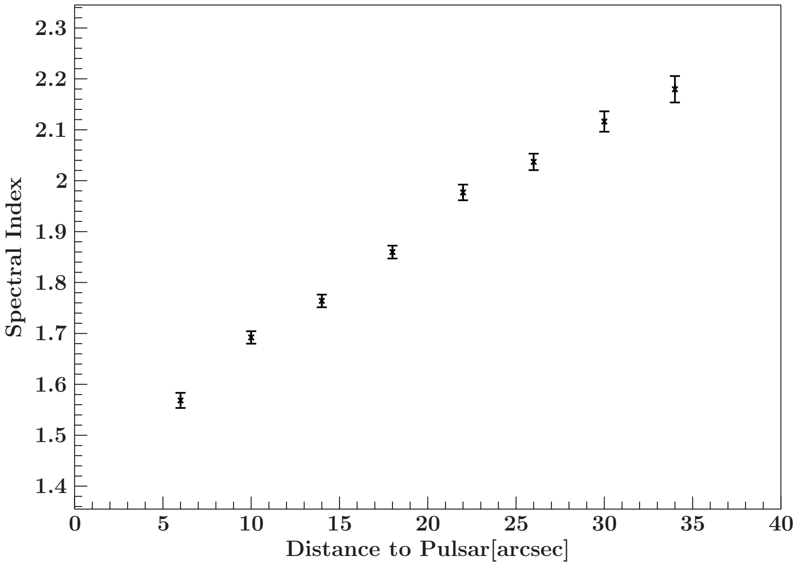

Fig. 4.7: *Evolution of fitted spectral index as a function of angular distance to the pulsar in the energy range of* $1-10\,\mathrm{keV}$.

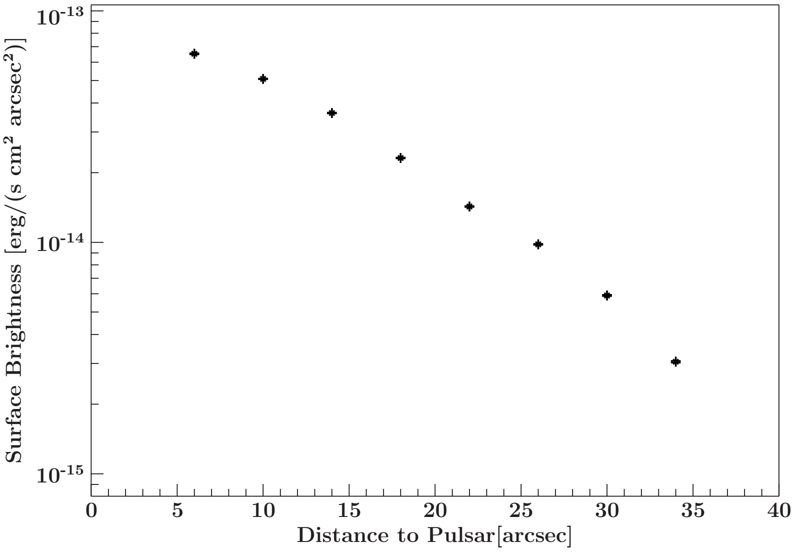

Fig. 4.8: *Evolution of the surface brightness as a function of angular distance to the pulsar in the energy range of* $1-10\,\mathrm{keV}$.

4.3 H. E. S. S.

G21.5−0.9 was observed not only in the X-ray part but also in the entire very-high-energy regime, e.g. with the H. E. S. S. experiment. Data from the H. E. S. S. experiment were analyzed using the Model++ analysis framework, which is based on the reconstruction and background discrimination techniques introduced by de Naurois & Rolland (2009). This technique compares the measured camera images with results from extensive Monte Carlo shower simulations. Using a log-likelihood method the properties of the initial photon, such as its direction and energy, are reconstructed.[9]

Very important is the correct treatment of the background. To avoid contamination by other γ-ray sources, regions where high emission is expected are excluded. For the reduction of the hadronic background one applies cuts on the signal. After defining the on-region, suitable off regions for the correct treatment of the background have to be found. Several background modeling methods have been established in very-high-energy γ-ray astronomy (see Berge et al. (2007)). The γ-ray excess in all models is defined as

$$N_{\text{excess}} = N_{\text{on}} - \alpha \times N_{\text{off}} \tag{4.1}$$

with the number of counts in the on-region N_{on}, the number of counts in the off-region N_{off} and the normalization factor α. α describes the differences in the solid angle, the exposure time, the zenith angle and the detector acceptance between on and off observations. The background model used in our analysis to create the maps is the *ring background* model where a ring-shaped region around the on-region is used for the estimation of the background. For the generation of the spectrum the *reflected* or *multiple off-regions background* model was applied, where a number of off-regions with the same size, the same shape and the same distance to the pointing position as the on-region is employed.

Commonly used spectral shapes are power law and modified power-laws like curved, broken or with exponential cut-off.[10]

In the following the results of our analysis are presented. The analysis was done with faint cuts, which are best suited for analyzing weak sources such as G21.5−0.9.[11] The first step was to make morphology fits using the database target position to determine the best-fit position. The chosen target position for the subsequent analysis is RA = 278.395° and DEC = −10.5617°. The θ^2, which is the square of the radius, of the on-region is 0.005 degree^2 which is the standard value for faint cuts and corresponds to a radius of $\approx 0.071\,°$, while for this analysis the 68 % containment radius of the point spread function is 0.06 °. The data was taken in 91 runs between 2004 and 2010 which corresponds to a total observation time of 38 hours and an acceptance-corrected live time of 24.1 hours. Except two 3-telescope observations all runs are 4-telescope observations. Fig. 4.9 shows the excess map, the significance map and the significance distribution. The latter on the right side shows the deviation from the background and that there is a significant source. As can be seen in the significance map the circle includes all regions above $5\,\sigma$.

---

[9] For a more detailed description the reader is referred to the mentioned article from de Naurois & Rolland (2009).

[10] In our analysis the power-law case was used, which is expressed as

$$\frac{\mathrm{d}N}{\mathrm{d}E} = \Phi_0 \left(\frac{E}{E_0}\right)^{-\alpha}, \tag{4.2}$$

where Φ_0 is the flux normalization, E_0 is the reference energy, which in most cases is typically chosen to be 1 TeV, and the differential spectral index α.

[11] Note that the ratio of signal to background obtained with standard cuts is 0.4, which is lower than the 0.7 achieved with faint cuts.

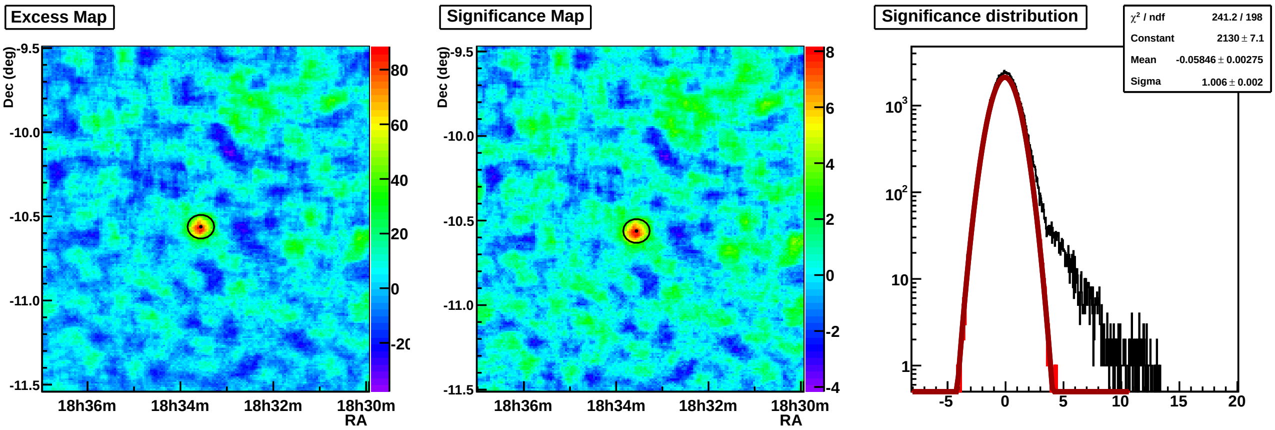

Fig. 4.9: *From left to right: Excess map, significance map and significance distribution from the H. E. S. S. analysis with faint cuts. The maps are oversampled with a radius* $r_{\mathrm{over}} = 0.06^\circ$.

Table 4.4: *Comparison of the parameters obtained with the ring and* reflected background.

<table>
<tr><th>Parameter</th><th><i>ring background</i></th><th><i>reflected background</i></th></tr>
<tr><td>acc. corr. live time [h]</td><td colspan="2">24.1</td></tr>
<tr><td>N_{on}</td><td colspan="2">219</td></tr>
<tr><td>N_{off}</td><td>3772</td><td>3926</td></tr>
<tr><td>α</td><td>29.93</td><td>30.98</td></tr>
<tr><td>excess counts</td><td>93.0</td><td>92.3</td></tr>
<tr><td>σ</td><td>7.3</td><td>7.3</td></tr>
</table>

The θ^2 plot of the analysis is depicted in Fig. 4.10. This plot shows the radial distance of the events to the test position for the *ring background*. The number of on and off-counts, $N_{\mathrm{on}} = 219$ and $N_{\mathrm{off}} = 3772$, are stated as well as the significance of $7.3\,\sigma$ (calculated following Li & Ma (1983), equation 17), and an α of 1/29.93.[12] Together with the excess map in Fig. 4.11 it can be clearly seen that G21.5−0.9 is a point-like source. Fig. 4.11 also shows the position of the pulsar PSR J1833−1034 and the target region of the H. E. S. S. analysis. Although there seems to be a small deviation between the pulsar position and the centre of the target region, they agree within the $3\,\sigma$ error.

The spectrum is, as already mentioned, obtained with the *reflected background*. The difference in the parameters between the *ring* and the *reflected background* can be seen in table 4.4.

The spectrum of G21.5−0.9 is shown in Fig. 4.12 fitted with a power law for the *reflected backgound*. The top part is the fit and the parameters of the fit are denoted in table 4.5. The results are compared with a published analysis by A. Djannati-Atai et al. (2007), where due to less available runs an acceptance corrected live time of 19.7 hours in comparison to our 24.1 hours was used. The fitted index is 2.31±0.21 which appears to be higher than the index of 2.08 ± 0.22 from A. Djannati-Atai et al. (2007) but is still compatible within the

---

[12] The α of 29.93 shown in Fig. 4.10 is the inverse of the α from equation 4.1 and therefore quoted as 1/29.93.

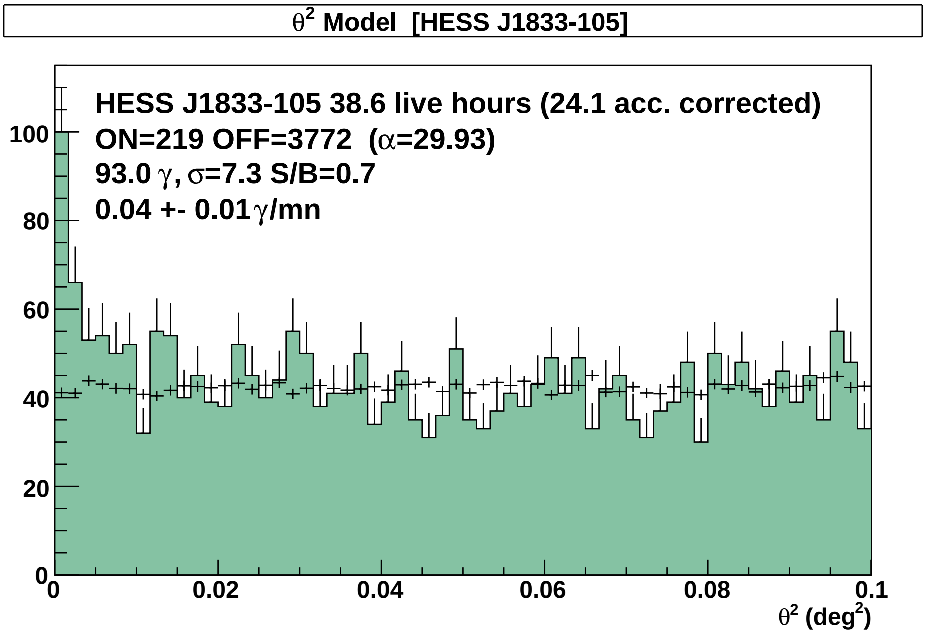

Fig. 4.10: *θ^2 plot of the H. E. S. S. analysis with faint cuts for the* ring background. *The strong peak in the first bin is a clear indication that G21.5−0.9 is a point-like source.*

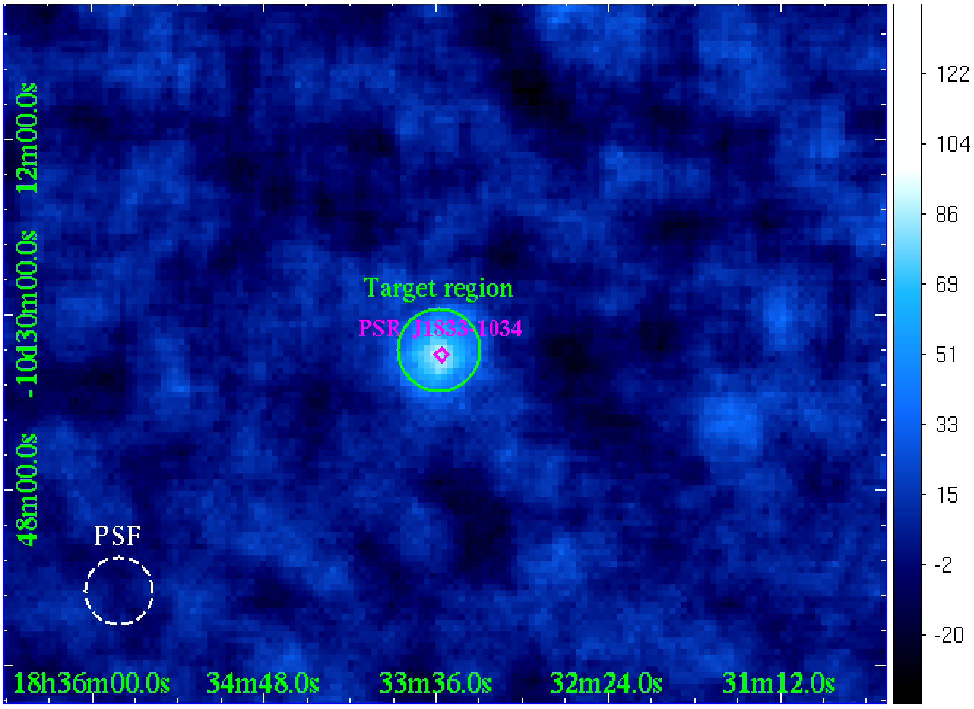

Fig. 4.11: *Excess map of the H. E. S. S. analysis with faint cuts and the test region for spectrum extraction in green, the position of the pulsar in magenta and the 68 % containment radius of the point spread function in white.*

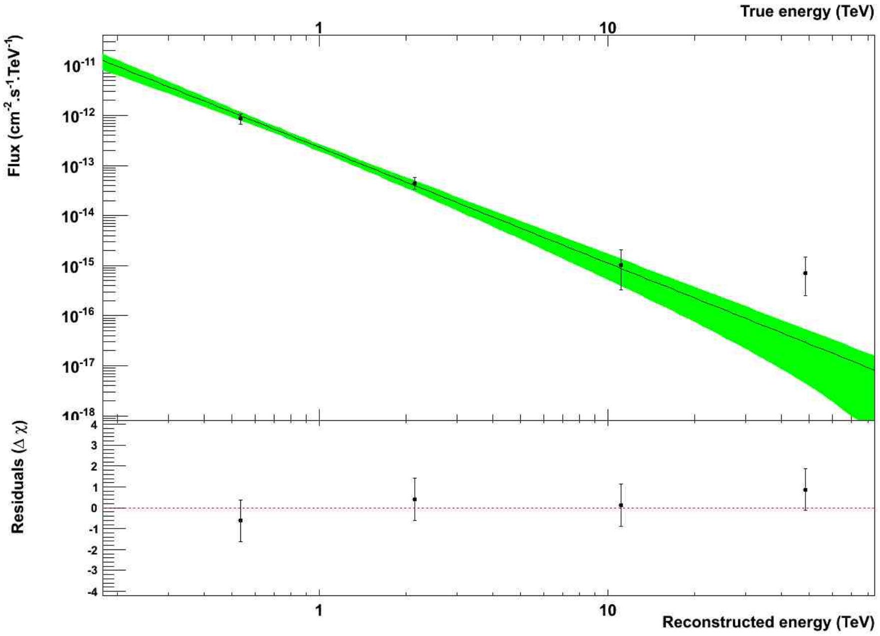

Fig. 4.12: *Power-law spectrum from the H. E. S. S. analysis with faint cuts showing the $3\,\sigma$ forward folded points.*

errors. The flux normalization at 1 TeV is $(2.33{\pm}0.39_{\mathrm{stat}}{\pm}0.47_{\mathrm{sys}}){\times}10^{-13}\,\mathrm{cm}^{-2}\ \mathrm{s}^{-1}\ \mathrm{TeV}^{-1}$, which is lower than the one obtained by A. Djannati-Atai et al. (2007). Note that the points are forward-folded points with a significance of $3\,\sigma$.[13] The bottom part depicts the residuals which show that the quality of the fit is quite well over the whole energy range.

Table 4.5: *Parameter results from the power-law fit to the H. E. S. S. data.*

Parameter	Result H. E. S. S. fit
Index	2.31 ± 0.21
Φ (1 TeV)	$(2.33 \pm 0.39) \times 10^{-13}\,\mathrm{cm}^{-2}\ \mathrm{s}^{-1}\ \mathrm{TeV}^{-1}$
Norm	$(0.40 \pm 0.07) \times 10^{-8}\,\mathrm{m}^{-2}\ \mathrm{s}^{-1}\ \mathrm{TeV}^{-1}$
I ($>$ 1 TeV)$^{(*)}$	$(1.77 \pm 0.49) \times 10^{-13}\,\mathrm{cm}^{-2}\ \mathrm{s}^{-1}$
Likelihood	-7.6
Equivalent χ^2	15.2/29 ndf
P	0.98

$^{(*)}$ integrated flux

---

[13] For more information on the forward-folding method see Piron et al. (2001).

5 Modeling of G21.5−0.9

In this chapter the leptonic model applied to G21.5−0.9 is described. The model is detailed in section 5.1. This model was introduced for the modeling of the PWN in MSH 15−52 by Schöck et al. (2010) and improved in the work of Holler et al. (2012) in its application to G0.9+0.1.[1] In section 5.2 the results of the parameter optimization are shown and the comparison with the outcome of the X-ray analysis is made, while in section 5.3 the modelled IC radiation is compared with H. E. S. S. data.

5.1 The model

Many different models aiming to describe the non-thermal emission from PWNe are published. Most of these models belong to the class of time-dependent models which try to reproduce the dynamical properties (e.g. van der Swaluw & Wu (2001)) while others are intended to predict the spectral properties (e.g. Volpi et al. (2008)). Moreover there are models which only apply to the initial expansion of the PWN (e.g. Del Zanna et al. (2004)) or which uses a semianalytic ansatz for the evolution (e.g. Gelfand et al. (2009)). The leptonic model used in this thesis is a spatially resolved and steady-state model, i.e. time-independent. One important characteristic of the model is the assumption of spherical symmetry. In comparison to the two PWNe investigated before G21.5−0.9 exhibits a particularly radially symmetric shape (see Fig. 2.4).
First we introduce the lepton injection spectra used in the model and then characterize the outward propagation of these leptons. Later we explain the parameter optimization and show how we compare the results of the modeling to measured data.

5.1.1 Lepton injection spectra

To model the emission of the PWN based on the radiation mechanisms explained in chapter 2 one needs to define the underlying lepton population. The starting point for this population is the wind termination shock where the particles are accelerated and injected into the PWN. We use two different lepton injection spectra that are described in the following.

5.1.1.1 Broken power law

It is widely assumed in the literature that the shape of the energy distribution of the injected population is a broken power law (see e.g. Kennel & Coroniti (1984b); Reynolds & Chevalier (1984)). The model concentrates on the inner part of the PWN where we suppose that the main contributors are young leptons. Therefore we assume that we can take the time-independent case because the time-scale of the modeling of the leptons

---

[1] For further details see the dissertation of F. Schöck (2010) and the diploma thesis of M. Holler (2010).

should be smaller than potential time variabilities in the injection spectrum. The broken power law in this time-independent case is denoted in the following form

$$Q_\mathrm{P}(E_\mathrm{e}) = \begin{cases} Q_{0,\mathrm{P}} \left(\dfrac{E_\mathrm{e}}{E_{\mathrm{b,P}}}\right)^{-p_1} & \text{for} \quad E_\mathrm{e} < E_{\mathrm{b,P}}, \\ Q_{0,\mathrm{P}} \left(\dfrac{E_\mathrm{e}}{E_{\mathrm{b,P}}}\right)^{-p_2} & \text{for} \quad E_\mathrm{e} \geq E_{\mathrm{b,P}}, \end{cases} \tag{5.1}$$

where E_e is the lepton energy, $E_{\mathrm{b,P}}$ is the break energy, p_1 and p_2 are the spectral indices and $Q_{0,\mathrm{P}}$ is the normalization.

We are only interested in the high-energy part of the spectrum as we investigate the X-ray and γ-ray regime of the spectrum. This restriction means that we can focus on energies higher than the break energy so that we can simplify equation 5.1 to:

$$Q_\mathrm{P}(E_\mathrm{e}) = Q_{0,\mathrm{P}} \left(\frac{E_\mathrm{e}}{E_\mathrm{b}}\right)^{-p}. \tag{5.2}$$

p replaces the index p_2 from equation 5.1.

To further simplify this equation one can define $Q_{0,\mathrm{P}}^{'} = Q_{0,\mathrm{P}} E_\mathrm{b}^p$ and work with a power-law spectrum of the form

$$Q_\mathrm{P}(E_\mathrm{e}) = Q_{0,\mathrm{P}}^{'} E_\mathrm{e}^{-p}, \tag{5.3}$$

which one may use as long as the energy range is above the break energy.

To determine the normalization of the injection spectrum we make use of the relation between the normalization and the spin-down luminosity,

$$\int_{E_{\mathrm{e,min}}}^{E_{\mathrm{e,max}}} Q_\mathrm{P}(E_\mathrm{e}) E_\mathrm{e} \, \mathrm{d}E_\mathrm{e} = \eta \dot{E}, \tag{5.4}$$

with the conversion efficiency η which describes how much spin-down luminosity is converted into the energy of the accelerated leptons. With equation 5.3 one gets

$$Q_{0,\mathrm{P}}^{'} \int_{E_{\mathrm{e,min}}}^{E_{\mathrm{e,max}}} E_\mathrm{e}^{-p+1} \, \mathrm{d}E_\mathrm{e} = \eta \dot{E}. \tag{5.5}$$

Integrating this equation and solving for $Q_{0,\mathrm{P}}^{'}$ yields

$$Q_{0,\mathrm{P}}^{'} = \begin{cases} \dfrac{\eta \dot{E}}{\ln\left(E_{\mathrm{e,max}}/E_{\mathrm{e,min}}\right)} & \text{for} \quad p = 2, \\ \dfrac{(2-p)\eta \dot{E}}{E_{\mathrm{e,max}}^{2-p} - E_{\mathrm{e,min}}^{2-p}} & \text{for} \quad p \neq 2. \end{cases} \tag{5.6}$$

It is possible to constrain some of the parameters in equation 5.6, which is done in section 5.1.1.3.

5.1.1.2 Maxwellian distribution with high-energy tail

The second lepton injection spectrum employed in this thesis was introduced by Spitkovsky (2008). The author used two-dimensional particle-in-cell simulations to study the shock structure in an unmagnetized plasma and derived a particle spectrum downstream of the termination shock that is comprised of a relativistic Maxwellian and a high-energy tail which consists of a power-law modified by an exponential cutoff. This solution is given by

$$Q_\mathrm{S}(E_\mathrm{e}) = \begin{cases} Q_{0,\mathrm{S1}} E_\mathrm{e} \exp\left(-\frac{E_\mathrm{e}}{\Delta E_1}\right) \\ \qquad\qquad \text{for } E_\mathrm{e} < E_{\mathrm{b,S}}, \\ Q_{0,\mathrm{S1}} E_\mathrm{e} \exp\left(-\frac{E_\mathrm{e}}{\Delta E_1}\right) + Q_{0,\mathrm{S2}} E_\mathrm{e}^{-\alpha_\mathrm{S}} \\ \qquad\qquad \text{for } E_{\mathrm{b,S}} \leq E_\mathrm{e} < E_\mathrm{cut}, \\ Q_{0,\mathrm{S1}} E_\mathrm{e} \exp\left(-\frac{E_\mathrm{e}}{\Delta E_1}\right) + Q_{0,\mathrm{S2}} E_\mathrm{e}^{-\alpha_\mathrm{S}} \exp\left(-\frac{E_\mathrm{e}-E_\mathrm{cut}}{\Delta E_\mathrm{cut}}\right) \\ \qquad\qquad \text{for } E_\mathrm{e} \geq E_\mathrm{cut}, \end{cases} \tag{5.7}$$

with the width of the relativistic Maxwellian ΔE_1, the break energy $E_{\mathrm{b,S}}$, the spectral index α_s, the cutoff energy E_cut, the cutoff width ΔE_cut and the normalizations $Q_{0,\mathrm{S1}}$ and $Q_{0,\mathrm{S2}}$. We adopt the values for the ratios $E_{\mathrm{b,S}}/\Delta E_1 \approx 7$, $E_\mathrm{cut}/E_{\mathrm{b,S}} \approx 7.5$ and $E_\mathrm{cut}/\Delta E_\mathrm{cut} \approx 3$ given in Spitkovsky (2008). Additionally we fix the value for α_s, which lies, according to Spitkovsky (2008), between 2.3 and 2.5, to 2.4.

Analogously to the power-law case one can calculate the normalization via the formula

$$\int_{E_{\mathrm{e,min}}}^{\infty} Q_\mathrm{S}(E_\mathrm{e}) E_\mathrm{e} \,\mathrm{d}E_\mathrm{e} = \eta \dot{E}. \tag{5.8}$$

Constraints of some of the parameters introduced until now are discussed in the next section.

5.1.1.3 Parameter constraints

To calculate Q_P or Q_S it is necessary to constrain the parameters. The spin-down luminosity $\dot{E}$ can be derived from measurements (see section 2.3) and for G21.5−0.9 it is $\dot{E} = 3.3 \times 10^{37}\,\mathrm{erg\ s^{-1}}$ (Camilo et al. 2006). The spectral index p is set to 2 to match the X-ray observations discussed in chapter 4. For the innermost annulus the spectral index is 1.569 ± 0.015. Assuming that the leptons do not lose much energy because of synchrotron radiation in that annulus one can use $p = 2\Gamma - 1$ to calculate p. To take the possible small synchrotron loss in account we use an index of $\Gamma = 1.5$ for the determination of p, which yields a value of 2. The conversion efficiency η is used as a free parameter for the optimization.

The next parameter to discuss is $E_{\mathrm{e,min}}$, the minimum lepton energy. As we consider the spectrum above the break energy one obvious choice would be $E_{\mathrm{e,min}} = E_\mathrm{b}$. However, this would lead to an unnecessary increase in computing time because typical break energies are too low for the production of high-energy particles anyhow. Instead, we use a value of $E_{\mathrm{e,min}} = 1\,\mathrm{erg}$ which is above typical break energies but also below energies that have an effect on the synchrotron emission or IC radiation in the observed energy ranges, as was shown by de Jager & Djannati-Ataï (2009).

In the case of the maximum lepton energy $E_{\mathrm{e,max}}$ there are two possible constraints: the gyroradius limit and the synchrotron limit.

The first one, the gyroradius limit, is based on the fact that the particle has to be inside the shock to be accelerated. This limit was introduced by Harding & Gaisser (1990). The gyroradius, also called Larmor radius, of the lepton with the highest energy has to be smaller than the shock radius R_S and is given by

$$r_\mathrm{L} = \frac{E_\mathrm{e,max}}{eB_\mathrm{S}} = \epsilon R_\mathrm{S}, \tag{5.9}$$

with the magnetic field strength at the shock B_S. The proportionality factor ϵ has to be smaller than 1. One can reform this equation to

$$E_\mathrm{e,max} = \epsilon e R_\mathrm{S} B_\mathrm{S}. \tag{5.10}$$

With the term for the magnetic field strength at the shock from Kennel & Coroniti (1984a)

$$B_\mathrm{S} = \frac{\kappa}{R_\mathrm{S}} \sqrt{\frac{\sigma}{1+\sigma} \frac{\dot{E}}{c}}\,, \tag{5.11}$$

where κ is the magnetic compression ratio and σ is the magnetization parameter, the expression for the maximum energy is given by

$$E_\mathrm{e,max} = \epsilon e \kappa \sqrt{\frac{\sigma}{1+\sigma} \frac{\dot{E}}{c}}, \tag{5.12}$$

where κ is the magnetic compression ratio and σ the magnetization parameter. This limit is important in the case of weak magnetic fields while in the case of a stronger magnetic field the synchrotron limit, which is described next, is relevant.

The synchrotron limit was introduced by de Jager et al. (1996). According to this article, particles on their way through a magnetic field reach their maximum energy when the synchrotron losses equal the total energy gain. This is denoted in the following equation where the first term describes the energy gain through first order Fermi acceleration and the second term characterizes the loss due to synchrotron radiation:

$$\frac{\mathrm{d}E_e}{\mathrm{d}t} = \frac{\alpha e B c}{2\pi} - \frac{2e^4 B^2 \gamma^2 \sin^2\theta}{3m_\mathrm{e}^2 c^3}. \tag{5.13}$$

α is a constant which depends on the shock geometry with a value ≤ 1 and θ is the pitch angle between the magnetic field and the direction of the particle. One can now calculate the maximum energy and de Jager et al. (1996) did that by setting $\frac{\mathrm{d}E_e}{\mathrm{d}t} = 0$ and solving the equation for $E_\mathrm{e,max}$,

$$E_\mathrm{e,max} = \gamma_\mathrm{max} m_\mathrm{e} c^2 = 1.9 \times 10^{13} \left(\frac{\alpha}{\langle \sin^2\theta \rangle B_\mathrm{G}} \right)^{1/2} \mathrm{eV}, \tag{5.14}$$

where B_G is the magnetic field strength in Gauss. When one assumes $\alpha = 1$ and $\langle \sin^2\theta \rangle = 1/2$ and converts the energy from keV to erg one obtains

$$E_\mathrm{e,max} = 43.84\, B_\mathrm{G}^{-1/2}\, \mathrm{erg}. \tag{5.15}$$

For the modeling both limits are calculated and the lower one of the two limits is used as $E_\mathrm{e,max}$ in the case of the power-law injection spectrum and as the cut-off energy in the case of the lepton injection spectrum from Spitkovsky (2008).

5.1.2 Propagation of the leptons

Having introduced the two lepton injection spectra, in this section we deal with the motion of the particles downstream of the termination shock. The goal is to derive expressions for the velocity and the magnetic field strength in order to be able to calculate those two parameters at any position within the PWN. The model implies spherical symmetry, and thus the velocity of the particles only depends on the radial distance to the termination shock and on the starting velocity at the shock. We adopt the velocity profile from Schöck et al. (2010) which was also used by Holler et al. (2012) and reads

$$v(r) = v_\mathrm{S}\left(\frac{R_\mathrm{S}}{r}\right)^{\alpha} . \tag{5.16}$$

v_S denotes the velocity at the termination shock and α denotes the index of the power-law which is a free parameter for the parameter optimization. In the before-mentioned references the authors adopt a value of $c/3$ for v_S. This comes from the determination of the shock velocity for the Crab Nebula in the work of Kennel & Coroniti (1984a). In our work v_S was left free in a region around this value of $c/3$.

In the case of the magnetic field strength we already used the equation 5.11 for the magnetic field strength at the shock B_S in the derivation of equation 5.12. The two quantities κ and σ are combined into a new parameter ξ which is left free for optimization

$$\xi = \kappa\sqrt{\frac{\sigma}{1+\sigma}} . \tag{5.17}$$

Inserting ξ into equation 5.11 yields

$$B_\mathrm{S} = \frac{\xi}{R_\mathrm{S}}\sqrt{\frac{\dot{E}}{c}} . \tag{5.18}$$

In the case of the ideal magnetohydrodynamic limit and a steady state, Kennel & Coroniti (1984a) showed that under the assumption of a toroidal magnetic field the following equation holds true:

$$Bvr = B_\mathrm{S} v_\mathrm{S} R_\mathrm{S} = \text{const}, \tag{5.19}$$

where v is the flow velocity, r the distance from the pulsar, B the magnetic field strength and the subscribed parameters correspond to the respective quantities at the shock. This formula can be rearranged to

$$B = \frac{B_\mathrm{S} v_\mathrm{S} R_\mathrm{S}}{vr} . \tag{5.20}$$

Inserting equation 5.16 yields the second required expression

$$B = B_\mathrm{S}\left(\frac{r}{R_\mathrm{S}}\right)^{\alpha-1} . \tag{5.21}$$

With these two equations (5.16 and 5.21) and the parameters R_S, α and ξ it is possible to calculate the velocity and magnetic field strength at any radial position r.

On their way through the PWN the particles lose energy due to adiabatic and synchrotron losses. By comparison, the losses because of IC radiation are negligible to the two mentioned mechanisms and therefore the total energy loss of the particles can be written in the following form:

$$\left(\frac{\mathrm{d}E}{\mathrm{d}t}\right)_\mathrm{total} = \left(\frac{\mathrm{d}E}{\mathrm{d}t}\right)_\mathrm{adiabatic} + \left(\frac{\mathrm{d}E}{\mathrm{d}t}\right)_\mathrm{synchrotron} . \tag{5.22}$$

The first term in this equation describes the total energy loss due to adiabatic expansion and can be written as derived by de Jager & Harding (1992):

$$\left(\frac{\mathrm{d}E}{\mathrm{d}t}\right)_{\text{adiabatic}} = -\frac{1}{3}E_e(\nabla\cdot\vec{v}). \tag{5.23}$$

Assuming the velocity is given by equation 5.16, the adiabatic term transforms to

$$\left(\frac{\mathrm{d}E_{\mathrm{e}}}{\mathrm{d}t}\right)_{\text{adiabatic}} = -\frac{1}{3}E_{\mathrm{e}}v_{\mathrm{S}}(2-\alpha)\frac{R_{\mathrm{S}}^{\alpha}}{r^{\alpha+1}}. \tag{5.24}$$

de Jager & Harding (1992) also discuss the second term, the synchrotron losses, which is expressed in the following formula:

$$\left(\frac{\mathrm{d}E_{\mathrm{e}}}{\mathrm{d}t}\right)_{\text{synchrotron}} = -2.368\times10^{-3}(BE_{\mathrm{e}})^2\,\mathrm{erg\,s^{-1}}. \tag{5.25}$$

5.1.3 Parameter optimization

Just as performed by Holler et al. (2012) the PWN is divided into a large number N_{shell} of concentric radial shells for the computation. With the equations for the lepton injection spectra and the energy loss introduced before, it is possible to propagate the lepton population outwards from shell to shell. $N_{\text{shell}} = 300$ was found to be appropriate as was shown in the diploma thesis of M. Holler (2010). In the two already mentioned references is explained how the three-dimensional shells are transformed to a smaller number of two-dimensional annuli to allow a comparison of the model with the X-ray analysis of the two-dimensional annuli. The number and the size of the annuli equals the annuli from the X-ray analysis. This transformation takes into account that only a part of the shell volume is visible in the projection represented by an annulus and that outer shells add up to the emission of an annulus.

The rest of this section shows how the measured data are compared with the data obtained from the model and describes constraints on the parameters.

5.1.3.1 Comparing measured and modeled data

To optimze the parameters it is necessary to find a way to not only compare the measured and the modeled data but also to get a numerical estimator to decide which set of parameters is the best. The method Schöck et al. (2010) used is to split the observed energy range (1-10 keV) into six energy bins of the same size. Comparing the modeled energy flux with the calculated one from the X-ray analysis in these six bins yields

$$X^2 = \sum_{\mathrm{i}=1}^{6}\left(\frac{F_{i,\mathrm{X-ray}} - F_{i,\mathrm{mod}}}{\Delta F_{i,\mathrm{X-ray}}}\right)^2, \tag{5.26}$$

where X^2 is the numerical estimator, $F_{i,\mathrm{X-ray}}$ and $F_{i,\mathrm{mod}}$ are the measured and modeled flux and $\Delta F_{i,\mathrm{X-ray}}$ is the statistical error in the corresponding energy bin.

We used a slightly different method implented by M. Holler after his diploma thesis, where one calculates X^2 for the index and the flux and adds them up for the total X^2. The splitting into six energy bins ($1-2.5\,\mathrm{keV}$, $2.5-4\,\mathrm{keV}$, $4-5.5\,\mathrm{keV}$, $5.5-7\,\mathrm{keV}$, $7-8.5\,\mathrm{keV}$

and $8.5 - 10\,\mathrm{keV}$) stays the same but one is only interested in the first and the last bin in order to calculate a X^2 for the index. Starting with the ratio of the energy flux from the first bin and the last, the sixth, bin of the measured data

$$R_{\mathrm{chandra,i}} = \frac{F_{\mathrm{chandra,i}}[1]}{F_{\mathrm{chandra,i}}[6]} \tag{5.27}$$

and from the modeled data

$$R_{\mathrm{model,i}} = \frac{F_{\mathrm{model,i}}[1]}{F_{\mathrm{model,i}}[6]}. \tag{5.28}$$

F denotes the energy flux, R the ratio, i the annulus and the number in square brackets gives the bin number. Applying the Gaussian propagation of errors to equation 5.27 yields

$$\Delta R_i = \sqrt{\left(\frac{\Delta F_{\mathrm{chandra,i}}[1]}{F_{\mathrm{chandra,i}}[6]}\right)^2 + \left(\frac{F_{\mathrm{chandra,i}}[1]\cdot \Delta F_{\mathrm{chandra,i}}[6]}{(F_{\mathrm{chandra,i}}[6])^2}\right)^2} \tag{5.29}$$

where $\Delta F_{\mathrm{chandra,i}}[1]$ is the error on the flux in the first bin of annulus i, the X^2 of the index is given by

$$X^2_{\mathrm{index}} = \sum_i \left(\frac{R_{\mathrm{chandra,i}} - R_{\mathrm{model,i}}}{\Delta R_{\mathrm{i}}}\right)^2. \tag{5.30}$$

Comparing the modeled and measured flux of an annulus in the full energy range from $1 - 10\,\mathrm{keV}$ yields

$$X^2_{\mathrm{flux}} = \sum_i \left(\frac{F_{\mathrm{chandra,i}} - F_{\mathrm{model,i}}}{\Delta F_{\mathrm{chandra,i}}}\right)^2 \tag{5.31}$$

The total X^2 value is given by

$$X^2_{\mathrm{chandra}} = X^2_{\mathrm{index}} + X^2_{\mathrm{flux}}. \tag{5.32}$$

To further improve the energy range of the model we included data from the *Integral* satellite which is sensitive in the hard X-ray regime. This data was taken from Tsujimoto et al. (2011) with an energy range from $15\,\mathrm{keV}$ to $50\,keV$. We splitted this energy range into three bins ($15 - 26.5\,\mathrm{keV}$, $26.5 - 38\,\mathrm{keV}$ and $38 - 50\,\mathrm{keV}$) and calculated the X^2 value in the following way:

$$X^2_{\mathrm{integral}} = \sum_{\mathrm{l=1}}^{3} \left(\frac{F_{l,\mathrm{integral}} - F_{l,\mathrm{mod}}}{\Delta F_{i,\mathrm{integral}}}\right)^2, \tag{5.33}$$

with the flux F, the error on the flux ΔF and l ranges from 1 to 3 for the bins. The X^2 value used to find the best parameter set is

$$X^2_{\mathrm{X-ray}} = X^2_{\mathrm{chandra}} + X^2_{\mathrm{integral}}. \tag{5.34}$$

5.1.3.2 Parameter constraints for the scan

The next step is to actually find the best parameter set. Due to strong correlations between several of the parameters, results of a fit would be of limited significance. Instead a parameter scan is performed and the first scan encompasses the physically allowed range. Of course one has to find constraints for the parameters before doing the first scan. As was mentioned in section 5.1.1.3 the spectral index p was set to 2. The first parameter to discuss is the shock radius R_{S}. Camilo et al. (2006) and Matheson & Safi-Harb (2010)

Table 5.1: *The range of parameters are shown for the parameter sets for which the X^2 value is at maximum 10 % higher than the lowest one. Note that not all combinations of parameters within these ranges lead to a low X^2 value.*

Parameter	Range power-law	Range Spitkovsky
R_{S} [arcsec]	2.5 – 3.0	2.5 – 3.5
v_{S}/c	0.18 – 0.38	0.33 – 0.58
ξ	0.06 – 0.16	0.16 – 0.185
ϵ	0.8 – 1.0	0.9 – 1
α	1.17 – 1.21	1.05 – 1.15
η	0.56 – 0.67	0.21 – 0.41

found values between $0''.9$ and $2''.0$. We decided to use values between $2''$ and $4''$. The upper limit of $4''$ was chosen because due to the good resolution of *Chandra* and the good exposure time one can can be sure that the termination shock is not larger than $4''$. The lower limit was set to $2''$ because with lower values the calculation fails. The next parameter to consider is the shock velocity v_{S} which was already discussed in section 5.1.2. We used a velocity in the range from $0.23c$ to $0.58c$. ξ was defined in equation 5.17 and depends on the compression ratio κ, which, folowing Kennel & Coroniti (1984b), lies between 1 and 3 and the magnetization parameter σ which should be smaller than 1. For the scan we allowed ξ to vary between 0 and 2.5. Another parameter is the index α of the velocity profile defined in equation 5.16. It should be larger than 0 and smaller than 2 because negative values would imply an acceleration beyond the shock and values larger than 2 an adiabatic energy gain. ϵ, the ratio of the Larmor radius and the shock radius, has to be smaller than 1 (see section 5.1.1.3) and we used ϵ between 0.6 and 1. Physical constraints limits the last parameter, the conversion efficiency η, to values between 0 and 1.

The step widths chosen for the parameters resulted in some ten thousands of parameter sets. For every one the X^2 was calculated. Then one concentrates on the range with the lowest X^2 and again makes a scan with plenty parameter sets. This is done until no further improvement of X^2 is found. All in all some hundred thousand sets were scanned. The results of this scan and the range of parameter values for the best parameter sets is presented in the next section.

5.2 Results of the modeling and comparison with the *Chandra* data

As was described in the previous section we did separate parameter scans for the two adopted lepton injection spectra. Because of the usage of a scan and not a fit and the limited precision of the calculation we obtain one best set of parameters but also some sets which have X^2 values of equal or less than 10 % higher values as the best one. Therefore we show a range of parameters for the best sets in table 5.1.

One can see that the results for the two different injection spectra vary in almost all parameters. The power-law injection spectrum seems to produce better results than the Maxwellian with high-energy tail. The best X^2 value for the Maxwellian with high-energy

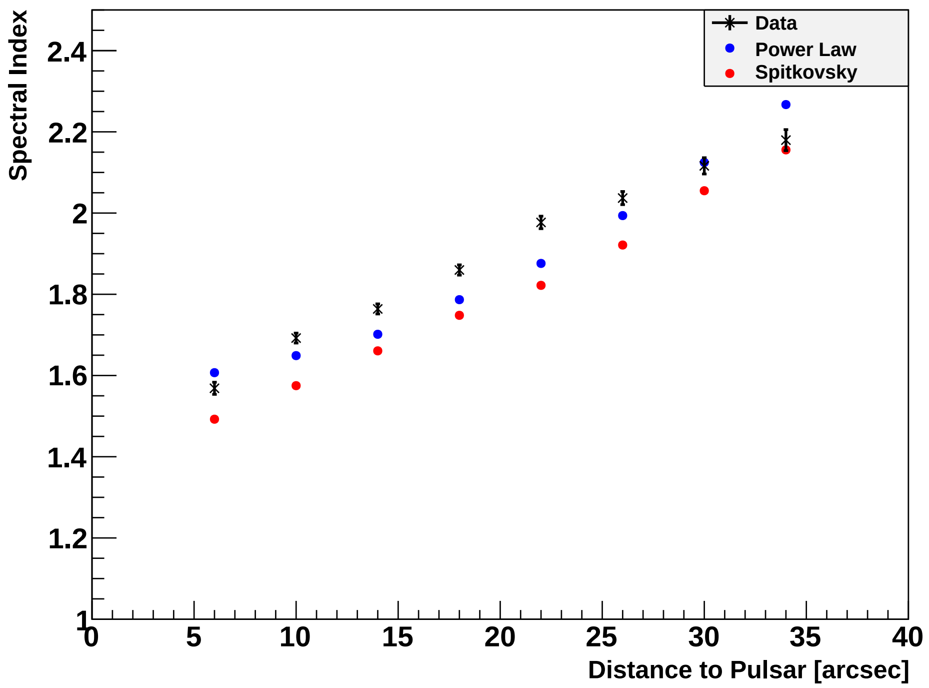

Fig. 5.1: *The measured spectral index is compared with the modeled spectral index for the two injection spectra. The X-ray data is shown in black, the model result for the power-law injection spectrum in blue and the model result for the injection spectrum from Spitkovsky (2008) in red.*

tail is approximately 1.6 times larger than the best X^2 value for the power law.

One of the aims of the model is to reproduce the evolution of the spectral index and the surface brightness obtained by the X-ray measurements. To check how well this is acomplished the measuered and modeled data are compared. We showed the results of the X-ray analysis in section 4.2.2 and use them for the comparison with the results of the model obtained with the best parameter set.

The comparison of the measured and modeled spectral index is shown in Fig. 5.1 where the index as a function of the radial distance to the pulsar is shown. For both injection spectra the index increases with distance but the shape differs from the measured data. For the Maxwellian with high-energy tail injection spectrum the index for the first annulus is too low while the difference gets smaller for the outer annuli. In the case of the power-law injection spectrum the deviation is smaller than in the previous case but there is still a difference in the shape compared to the measured data.

We find a better match when we compare the surface brightness as can be seen in Fig. 5.2. The modeled surface brightness for both injection scenarios is in a very good agreement with the measured one. There are two deviations clearly visible. The first one is the too high value for the Spitkosky spectrum in the innermost annulus and the too low values for both spectra in the outermost annulus. The latter reflects the fact that the model is better suited for the inner part of the PWN.

With equations 5.21 and 5.18 one can calculate the magnetic field strength. For the best

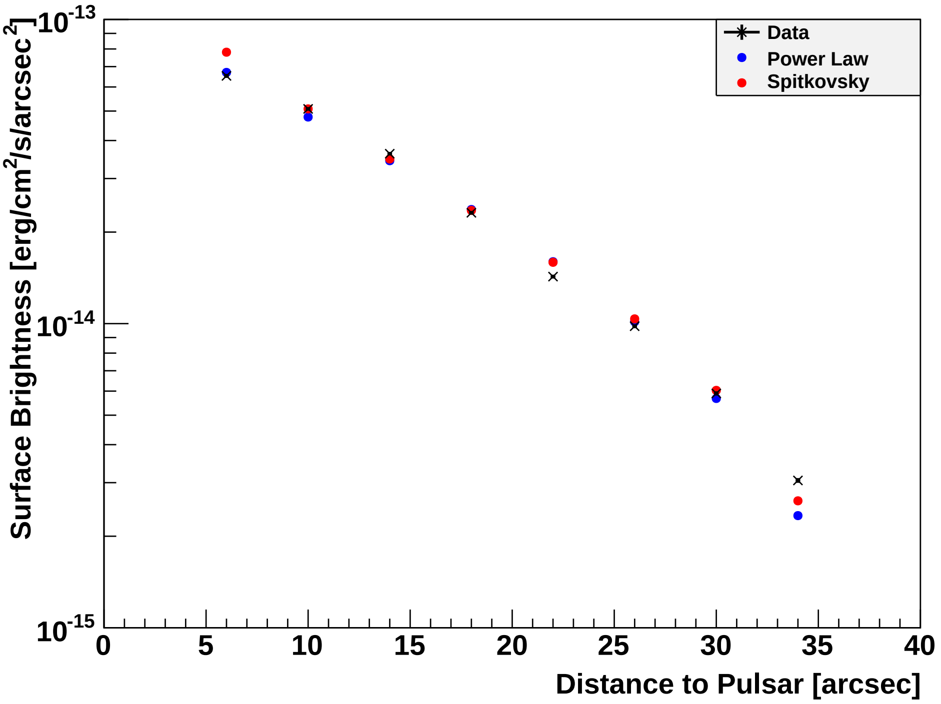

Fig. 5.2: *The measured surface brightness is compared with the modeled surface brightness for the two injection spectra. The X-ray data is shown in black, the model result for the power-law injection spectrum in blue and the model result for the injection spectrum from Spitkovsky (2008) in red.*

parameter sets, i.e. at maximum 10 % higher X^2 than the lowest one, the magnetic field strength lies between 13 μG and 29 μG. This is in good agreement with a value of 25 μG estimated by de Jager et al. (2008). However, Tanaka & Takahara (2011), using a one-zone time-dependent model, found a slightly higher magnetic field strength of 64 μG for model 1 and 47 μG for model 2 which they still claim to be consistent with the result from de Jager et al. (2008).
All in all, the match between the measured and the modeled data is still not perfect yet, but already very well.

5.3 Comparison with the H. E. S. S. results

A second aim of the modelling is to make a prediction for the γ-ray regime and compare this prediction with measured H. E. S. S. data. This is done by assuming that the same leptons that are responsible for the synchrotron emission also scatter up low-energy photons to the VHE regime due to the IC effect. Hence it is possible to calculate the IC flux and compare it with the H. E. S. S. measurement. There are three different seed photon fields potentially contributing to the IC radiation: these photons can come from the CMB, IR photons from local dust or from local starlight. The CMB is best described by a blackbody distribution with 2.725 K. The other two photon fields are not that easy to describe in a general way. The estimation of the interstellar radiation fields from Porter & Strong (2005) was used which were developed for the GALPROP code from Strong et al. (2000).

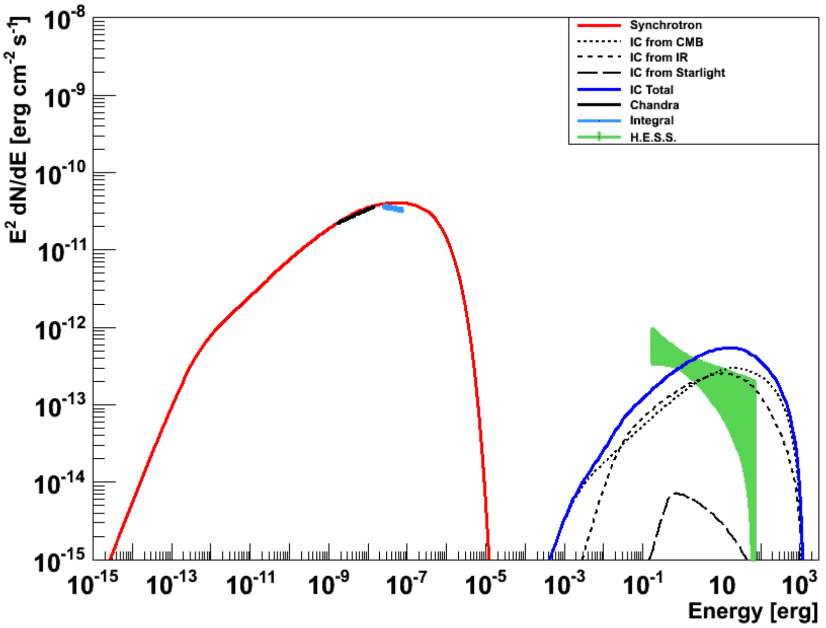

Fig. 5.3: *SED for G21.5−0.9, with the power-law injection spectrum, showing the calculated IC radiation compared to the H. E. S. S. data from our own analysis. The measured Chandra data and the Integral data are also included.*

The better X^2 values for the power-law injection spectrum are only partly reflected in the SEDs, which are shown in Fig. 5.3 and Fig. 5.4 for the power-law injection spectrum and the one from Spitkovsky (2008), respectively. The two injection spectra differ in the lower energy part (X-rays) and in the high-energy part (γ-ray). While the power-law case results in a better match with the experimental X-ray data, the other case comes closer to what is measured in the γ-ray regime. One explanation for the deviation in the γ-ray regime is the assumption that the same lepton population that is responsible for the synchrotron emission is also responsible for the IC radiation. The assumption forms a simplification since also older lepton populations contribute to the IC radiation. Furthermore different source sizes in the individual energy regimes may add to the deviation: according to the X-ray analysis, in the keV regime, the radius of the PWN is 36″. In TeV γ-rays G21.5−0.9 is seen as a point source which, considering the poorer energy resolution of H. E. S. S. compared to the X-ray satellites, means that the on-source region is larger. Therefore it is not expected that the model is able to predict the results from the H. E. S. S. analysis accurately. The built-in assumption of the steady state limits the model to small spatial regions and hence it is not straightforward to extend the model to accommodate also larger regions such as G21.5−0.9 seen with H. E. S. S. Another source of uncertainty in the calculation of the IC radiation stems from the seed photon fields, which may exhibit strong local variations.

Potential future improvements would be the implementation of a time-dependence and a more realistic toroidal magnetic field. The agreement between results from γ-ray telescopes with the prediction from the modeling should get better with these features although they only aim to amend the first of the three mentioned problems and do not touch upon size or seed photon fields problem.

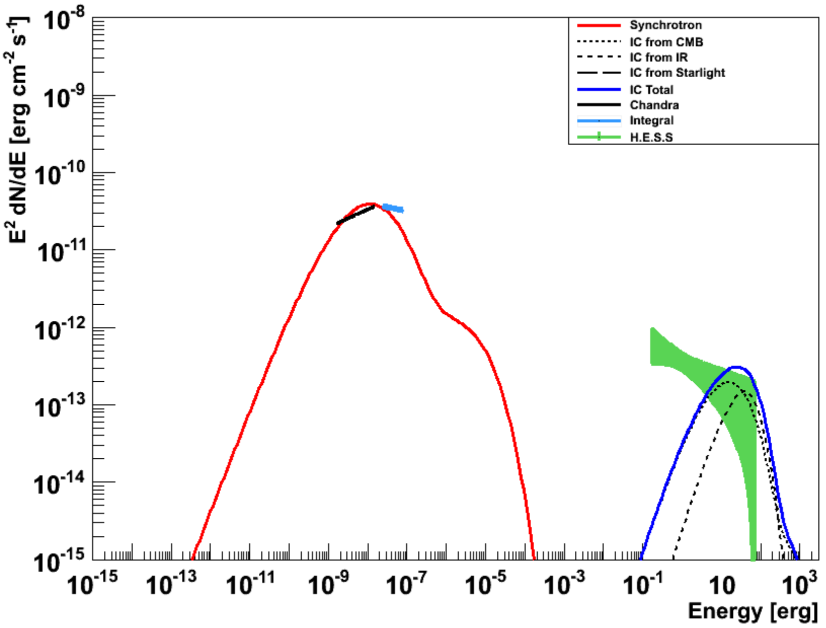

Fig. 5.4: *SED for G21.5−0.9, with the injection spectrum from Spitkovsky (2008), showing the calculated IC radiation compared to the H. E. S. S. data from our own analysis. The measured Chandra data and the Integral data are also included.*

6 Conclusion

The aim of this thesis was to perform a detailed analysis of the non-thermal emission from the pulsar wind nebula in the supernova remnant G21.5−0.9. An important motivation for observing and studying PWNe is the aim to understand the mechanisms that allow to accelerate particles up to the very-high-energy regime. One way to do this is to model particle population and the corresponding non-thermal emission, and to compare the results with the measurements. The model used in this thesis is a radially symmetric, time-independent leptonic model.

The first part of this thesis comprises a general introduction to PWNe and the related radiation mechanisms. Our current view on G21.5−0.9 and the associated pulsar PSR J1833-1034 is presented. One major difference to the PWNe MSH 15−52 and G0.9+0.1, which were investigated in earlier works with the same model, is the exceptional degree of radial symmetry manifested in X-ray observations of the PWN G21.5−0.9, which seems to vindicate the usage of a radially symmetric model. The model uses information obtained in an X-ray analysis of the inner part of the PWN to find the values of the free parameters of the model. These parameters are optimized by comparing the measured data with the results from the calculation of synchrotron radiation. For this analysis data from one *XMM-Newton* and 66 *Chandra* observations were analyzed to determine the absorption column density nH. To investigate the spectral properties of the PWN, the central region from $4''$ to $36''$ was divided into eight concentric annuli and the *Chandra* data were analyzed for each annulus. The spectrum for each observation was generated separately, and subsequently all individual spectra were fitted simultaneously with an absorbed power law. The results of the X-ray analysis show an increasing spectral index from 1.57 in the innermost annulus to 2.20 in the outer annulus, reflecting a spectral softening of the emission, and a decreasing surface brightness with larger distance to the pulsar. On the very-high-energy side, an analysis of data obtained with the H. E. S. S. experiment was carried out and the results are presented.

In the next step, our leptonic model was used in order to reproduce the measured properties – spectral index and surface brightness – and to make a prediction for the Inverse Compton contribution to the very-high-energy emission. The parameter optimization was done with a scan and not a fit because of the highly correlated parameters, and for each parameter the range of the best values is given. With these optimized parameters the model is able to reproduce the spectral index and the surface brightness nicely. Assuming the same lepton population producing the synchrotron emission is also producing the Inverse Compton radiation, the latter is calculated with the best parameters found before. The radiation is then compared with results from the H. E. S. S. experiment. The comparison does not favour either of the two adopted injection spectra. Although the obtained flux is on the same order of magnitude as the measured one, the spectral shape differs in both cases. However, a small deviation in the shape is expected as the assumption made before is only partly true because presumably also older populations contribute to the Inverse Compton radiation.

To further improve the model and therefore the prediction for the γ-ray regime, a time dependence or a more realistic toroidal magnetic field could be implemented in the future.

List of Figures

List of Tables

Bibliography

A. Djannati-Atai, De Jager, O. C., Terrier, R., Gallant, Y. A., & Hoppe, S. 2007, ArXiv e-prints 0710.2247

Abdo, A. A., Ackermann, M., Ajello, M., et al. 2011, ApJ, 726, 43

Aharonian, F. A. & Bogovalov, S. V. 2003, New Astronomy, 8, 85

Anders, E. & Grevesse, N. 1989, Geochim. Cosmochim. Acta, 53, 197

Arnaud, M., Neumann, D. M., Aghanim, N., et al. 2001, A&A, 365, L80

Balucinska-Church, M. & McCammon, D. 1992, ApJ, 400, 699

Becker, R. H. & Kundu, M. R. 1976, ApJ, 204, 427

Berge, D., Funk, S., & Hinton, J. 2007, A&A, 466, 1219

Bietenholz, M. F. & Bartel, N. 2008, MNRAS, 386, 1411

Bietenholz, M. F., Matheson, H., Safi-Harb, S., Brogan, C., & Bartel, N. 2011, MNRAS, 412, 1221

Blackburn, J. K. 1995, in Astronomical Society of the Pacific Conference Series, Vol. 77, Astronomical Data Analysis Software and Systems IV, ed. R. A. Shaw, H. E. Payne, & J. J. E. Hayes, 367

Blumenthal, G. R. & Gould, R. J. 1970, Reviews of Modern Physics, 42, 237

Bocchino, F., van der Swaluw, E., Chevalier, R., & Bandiera, R. 2005, A&A, 442, 539

Camilo, F., Ransom, S. M., Gaensler, B. M., et al. 2006, ApJ, 637, 456

de Jager, O. C. & Djannati-Ataï, A. 2009, in Astrophysics and Space Science Library, Vol. 357, Astrophysics and Space Science Library, ed. W. Becker, 451

de Jager, O. C., Ferreira, S. E. S., & Djannati-Ataï, A. 2008, in American Institute of Physics Conference Series, Vol. 1085, American Institute of Physics Conference Series, ed. F. A. Aharonian, W. Hofmann, & F. Rieger, 199–202

de Jager, O. C. & Harding, A. K. 1992, ApJ, 396, 161

de Jager, O. C., Harding, A. K., Michelson, P. F., et al. 1996, ApJ, 457, 253

de Naurois, M. & Rolland, L. 2009, Astroparticle Physics, 32, 231

Del Zanna, L., Amato, E., & Bucciantini, N. 2004, A&A, 421, 1063

den Herder, J. W., Brinkman, A. C., Kahn, S. M., et al. 2001, A&A, 365, L7

Furst, E., Handa, T., Morita, K., et al. 1988, PASJ, 40, 347

Gaensler, B. M. & Slane, P. O. 2006, ARA&A, 44, 17

Garmire, G. P., Bautz, M. W., Ford, P. G., Nousek, J. A., & Ricker, Jr., G. R. 2003, in Society of Photo-Optical Instrumentation Engineers (SPIE) Conference Series, Vol. 4851, Society of Photo-Optical Instrumentation Engineers (SPIE) Conference Series, ed. J. E. Truemper & H. D. Tananbaum, 28–44

Gelfand, J. D., Slane, P. O., & Zhang, W. 2009, ApJ, 703, 2051

Gotthelf, E. V. 2004, in IAU Symposium, Vol. 218, Young Neutron Stars and Their Environments, ed. F. Camilo & B. M. Gaensler, 225

Gupta, Y., Mitra, D., Green, D. A., & Acharyya, A. 2005, Current Science, 89, 853

Hanke, M. 2011, Dissertation, Probing the Environment of Accreting Compact Objects, Friedrich-Alexander-Universität, Erlangen, Germany

Harding, A. K. & Gaisser, T. K. 1990, ApJ, 358, 561

Hinton, J. A. & Hofmann, W. 2009, ARA&A, 47, 523

Holler, M. 2010, Diploma thesis, Spatially Resolved X-Ray Analysis and Modeling of the Non-Thermal Emission of the Pulsar Wind Nebula G0.9+0.1, Friedrich-Alexander-Universität, Erlangen, Germany

Holler, M., Schöck, F. M., Eger, P., et al. 2012, A&A, 539, A24

Joye, W. A. & Mandel, E. 2003, in Astronomical Society of the Pacific Conference Series, Vol. 295, Astronomical Data Analysis Software and Systems XII, ed. H. E. Payne, R. I. Jedrzejewski, & R. N. Hook, 489

Kennel, C. F. & Coroniti, F. V. 1984a, ApJ, 283, 694

Kennel, C. F. & Coroniti, F. V. 1984b, ApJ, 283, 710

Li, T.-P. & Ma, Y.-Q. 1983, ApJ, 272, 317

Lumb, D. H., Schartel, N., & Jansen, F. A. 2012, ArXiv e-prints 1202.1651

Majerowicz, S., Neumann, D. M., & Reiprich, T. H. 2002, A&A, 394, 77

Mason, K. O., Breeveld, A., Much, R., et al. 2001, A&A, 365, L36

Matheson, H. & Safi-Harb, S. 2005, Advances in Space Research, 35, 1099

Matheson, H. & Safi-Harb, S. 2010, ApJ, 724, 572

Piron, F., Djannati-Atai, A., Punch, M., et al. 2001, A&A, 374, 895

Porter, T. A. & Strong, A. W. 2005, in International Cosmic Ray Conference, Vol. 4, International Cosmic Ray Conference, 77

Reynolds, S. P. & Chevalier, R. A. 1984, ApJ, 278, 630

Safi-Harb, S., Harrus, I. M., Petre, R., et al. 2001, ApJ, 561, 308

Schöck, F. M. 2010, Dissertation, A detailed Study of the Pulsar Wind Nebula MSH 15-5*2* in X-rays and TeV γ-rays, Friedrich-Alexander-Universität, Erlangen, Germany

Schöck, F. M., Büsching, I., de Jager, O. C., Eger, P., & Vorster, M. J. 2010, A&A, 515, A109

Slane, P., Chen, Y., Schulz, N. S., et al. 2000, ApJ, 533, L29

Spitkovsky, A. 2008, ApJ, 682, L5

Strong, A. W., Moskalenko, I. V., & Reimer, O. 2000, ApJ, 537, 763

Strüder, L., Briel, U., Dennerl, K., et al. 2001, A&A, 365, L18

Tanaka, S. J. & Takahara, F. 2011, ApJ, 741, 40

Tian, W. W. & Leahy, D. A. 2008, MNRAS, 391, L54

Tsujimoto, M., Guainazzi, M., Plucinsky, P. P., et al. 2011, A&A, 525, A25

Turner, M. J. L., Abbey, A., Arnaud, M., et al. 2001, A&A, 365, L27

van der Swaluw, E. & Wu, Y. 2001, ApJ, 555, L49

Verner, D. A., Ferland, G. J., Korista, K. T., & Yakovlev, D. G. 1996, ApJ, 465, 487

Volpi, D., Del Zanna, L., Amato, E., & Bucciantini, N. 2008, A&A, 485, 337

Warwick, R. S., Bernard, J.-P., Bocchino, F., et al. 2001, A&A, 365, L248

Weisskopf, M. C., Brinkman, B., Canizares, C., et al. 2002, PASP, 114, 1

Wilms, J., Allen, A., & McCray, R. 2000, ApJ, 542, 914

Wolter, H. 1952, Annalen der Physik, 445, 94

Zajczyk, A., Gallant, Y. A., Slane, P., et al. 2011, ArXiv e-prints 1105.4373

Danksagung

Da eine Diplomarbeit nicht ohne die Hilfe anderer möglich ist, möchte ich die Gelegenheit nutzen einigen Personen zu danken.

- Prof. Dr. Christian Stegmann für die Vergabe dieses tollen Themas und die Möglichkeit beim Spiegelaustausch teilzunehmen.
- Dr. Kathrin Valerius, Markus Holler und Dr. Peter Eger für die hervorragende Betreuung und Beantwortung vieler, vieler Fragen während der Diplomarbeit. An Markus und vor allem Kathrin auch für das unermüdliche Korrekturlesen meiner Arbeit.
- Der kompletten H. E. S. S. Gruppe in Erlangen (sowohl den aktuellen als auch den mittlerweile ehemaligen Mitgliedern) für die tolle Arbeitsatmosphäre und die netten Pausen.
- Dr. Felix Fürst und Prof. Dr. Jörn Wilms für die Unterstützung bei der *Chandra*-Analyse.
- Steffi, Neli und Michi für die sehr angenehme Büroatmosphäre und das Beantworten von anfangs vielen Fragen eines Neudiplomanden.
- Meiner Familie (vor allem meinen Eltern) ohne deren Unterstützung in jedweder Art weder das Studium noch die Diplomarbeit in der Form möglich gewesen wäre.

Erklärung

Ich bestätige hiermit, dass ich die vorliegende Diplomarbeit selbständig verfasst und keine anderen als die angegebenen Quellen und Hilfsmittel verwendet habe.

Erlangen, den 23. Mai 2012